A new model to simulate the Martian mesoscale and microscale atmospheric circulation: Validation and first results

Aymeric Spiga[1] and François Forget[1]

[1] The Laboratoire de Météorologie Dynamique (LMD) Mesoscale Model is a new versatile simulator of the Martian atmosphere and environment at horizontal scales ranging from hundreds of kilometers to tens of meters. The model combines the National Centers for Environmental Prediction(NCEP)-National Center for Atmospheric Research (NCAR) fully compressible nonhydrostatic Advanced Research Weather Research and Forecasting (ARW-WRF) dynamical core, adapted to Mars, with the LMD-general circulation model (GCM) comprehensive set of physical parameterizations for the Martian dust, CO_2, water, and photochemistry cycles. Since LMD-GCM large-scale simulations are also used to drive the mesoscale model at the boundaries of the chosen domain of interest, a high level of downscaling consistency is reached. To define the initial state and the atmosphere at the domain boundaries, a specific "hybrid" vertical interpolation from the coarse-resolution GCM fields to the high-resolution mesoscale domain is used to ensure the stability and the physical relevancy of the simulations. Used in synoptic-scale mode with a cyclic domain wrapped around the planet, the mesoscale model correctly replicates the main large-scale thermal structure and the zonally propagating waves. The model diagnostics of the near-surface pressure, wind, and temperature daily cycles in Chryse Planitia are in accordance with the Viking and Pathfinder measurements. Afternoon gustiness at the respective landing sites is adequately accounted for on the condition that convective adjustment is turned off in the mesoscale simulations. On the rims of Valles Marineris, intense daytime anabatic ($\sim$30 m s^{-1}) and nighttime katabatic ($\sim$40 m s^{-1}) winds are predicted. Within the canyon corridors, topographical channeling can amplify the wind a few kilometers above the ground, especially during the night. Through large-eddy simulations in Gusev Crater, the model describes the mixing layer growth during the afternoon, and the associated dynamics: convective motions, overlying gravity waves, and dust devil–like vortices. Modeled temperature profiles are in satisfactory agreement with the Miniature Thermal Emission Spectrometer (Mini-TES) measurements. The ability of the model to transport tracers at regional scales is exemplified by the model's prediction for the altitude of the Tharsis topographical water ice clouds in the afternoon. Finally, a nighttime "warm ring" at the base of Olympus Mons is identified in the simulations, resulting from adiabatic warming by the intense downslope winds along the flanks of the volcano. The surface temperature enhancement reaches +20 K throughout the night. Such a phenomenon may have adversely affected the thermal inertia derivations in the region.

1. Introduction

[2] The Mars Global Surveyor (MGS) mission yielded unprecedented observations of Martian meteorological phenomena at various horizontal scales below 100 km [e.g., *Wang and Ingersoll*, 2002]. This was the starting point of numerous modeling efforts to accurately simulate regional processes unresolvable by the Martian Global Climate Models (or general circulation models, hereinafter referred as GCM). Indeed, even if idealized 1-D or 2-D models had provided interesting diagnostics of the planetary boundary layer [*Haberle et al.*, 1993; *Savijärvi et al.*, 2004], the slope winds [*Ye et al.*, 1990; *Savijärvi and Siili*, 1993] and the lee waves [*Pickersgill and Hunt*, 1981; *Tobie et al.*, 2003], they lacked the fully three-dimensional representation of the Martian atmosphere at local scales.

[3] *Rafkin et al.* [2001], *Tyler et al.* [2002], and *Toigo and Richardson* [2002] built such three-dimensional Martian models by coupling state-of-the-art terrestrial regional climate models with physical parameterizations of the Martian

[1]Laboratoire de Météorologie Dynamique, Institut Pierre-Simon Laplace, Ecole Polytechnique, Université Pierre et Marie Curie, Centre National de la Recherche Scientifique, Paris, France.

environment initially developed for the Martian GCMs. These efforts gave birth to powerful simulators of the Martian atmospheric circulations at the mesoscale (hundreds of kilometers to 1 km) and the microscale (1 km to hundreds of meters). Alternative Martian mesoscale models were later developed by *Siili et al.* [2006] and *Wing and Austin* [2006]. Mesoscale meteorological diagnostics could be derived as well from GCMs that include adaptable-grid zooming capabilities [*Forget et al.*, 1999a; *Moudden and McConnell*, 2005]. As was demonstrated recently by *Richardson et al.* [2007], mesoscale dynamical solvers can also be turned into fully operable GCMs, while keeping the ability to be employed for regional-scale applications.

[4] The 3-D Martian mesoscale models have refined the analysis of the aforementioned idealized studies. The intense thermal circulations underlying the formation of spectacular water ice clouds [*Michaels et al.*, 2006] and spiral dust plumes [*Rafkin et al.*, 2002] on the Tharsis volcanoes were comprehensively accounted for. Specific studies assessing the transient eddies [*Tyler and Barnes*, 2005] and dust storms [*Toigo et al.*, 2002] occurring at the edges of the polar caps were also carried out. The first large-eddy simulations for Mars were performed to assess the structure of the Martian boundary layer [*Michaels and Rafkin*, 2004; *Tyler et al.*, 2006; *Richardson et al.*, 2007] and the formation of "dust devil–like" convective vortices [*Toigo et al.*, 2003]. All these studies demonstrate that the Martian atmospheric circulation at the mesoscale and the microscale is highly energetic, owing to high thermal contrasts, short radiative time scales, low atmospheric density and steep topographical gradients. The recent high-resolution observations by the Mars Reconnaissance Orbiter (MRO) [*Malin et al.*, 2008] offer new challenges for mesoscale modelers.

[5] Apart from broadening the knowledge of the atmospheric circulation on Mars, the Martian mesoscale models have been of practical utility to investigate the local aeolian processes involved in the formation of geological features such as dunes or streaks [*Kuzmin et al.*, 2001; *Fenton et al.*, 2005; *Greeley et al.*, 2008]. They have also been employed to estimate the atmospheric hazards at the selected landing sites of the Mars Exploration Rovers (MER) [*Toigo and Richardson*, 2003; *Rafkin and Michaels*, 2003] and Beagle 2 [*Rafkin et al.*, 2004], and provided guidance to design the MER Entry, Descent and Landing system [*Kass et al.*, 2003]. The need for accurate and realistic Martian mesoscale modeling is still critical for the design of upcoming missions to Mars (e.g., Mars Science Laboratory, ExoMars).

[6] The purpose of this paper is to describe and validate a new Martian mesoscale model developed at the Laboratoire de Météorologie Dynamique (LMD). The model is novel in the sense that it combines (1) the recent improvements in the stability, accuracy and ergonomy of the mesoscale dynamical solvers developed for terrestrial applications [*Skamarock et al.*, 2005; *Skamarock and Klemp*, 2008] and (2) the entire state-of-the-art Martian parameterizations developed for nearly two decades in the LMD Martian GCM (LMD-MGCM) to describe the CO_2 cycle [*Hourdin et al.*, 1993], the dust cycle [*Forget et al.*, 1999a], the water cycle [*Montmessin et al.*, 2004], and the photochemical cycles [*Lefèvre et al.*, 2004]. In addition to the obvious advantages of this virtuous association, the use of the same Martian physical parameterizations both in the mesoscale model, and in the GCM that is providing initial and boundary conditions to the mesoscale model, ensures a high level of downscaling consistency.

2. Model Description
2.1. Dynamical Core

[7] The numerical integration of the atmospheric fluid dynamic equations is performed in meteorological models by the dynamical core. The LMD Martian Mesoscale Model dynamical core is based on the stable and carefully tested, fully parallellized, Advanced Research Weather Research and Forecasting model (hereinafter referred as ARW-WRF) [*Skamarock et al.*, 2005; *Skamarock and Klemp*, 2008], developed for terrestrial applications at National Centers for Environmental Prediction (NCEP)-National Center for Atmospheric Research (NCAR) (version 2.2.1, November 2007).

[8] The ARW-WRF mesoscale model integrates the fully compressible nonhydrostatic Navier-Stokes equations in a specific area of interest on the planet. Since the mesoscale models can be employed to resolve meteorological motions less than few kilometers, a scale at which the vertical wind acceleration might become comparable to the acceleration of gravity, hydrostatic balance cannot be assumed, as is usually done in GCMs.

[9] Mass, momentum, entropy, and tracer conservation are ensured by an explicitly conservative flux-form formulation of the fundamental equations, based on mass-coupled meteorological variables (winds, potential temperature, tracers). Alternatively, these variables are recast into a reference profile plus a perturbation to reduce truncation errors [*Skamarock and Klemp*, 2008]. Tracer transport can be computed by an additional forward-in-time scheme based on the Piecewise Parabolic Method [*Carpenter et al.*, 1990], with positive definite and monotonic properties [*Skamarock*, 2006].

[10] In the vertical dimension, the equations are projected, as suggested by *Laprise* [1992], on terrain-following mass-based coordinates ("eta levels"): $\eta = (\pi - \pi_t)/(\pi_s - \pi_t)$ where π is the hydrostatic component of the pressure, π_s the value at the surface and π_t the (constant) upper boundary value. As shown by *Laprise* [1992] and *Janjic et al.* [2001], the choice of such vertical coordinates enables the integration of the ARW-WRF equations either in full nonhydrostatic mode or under the hydrostatic assumption. At the top of the domain, a free relaxation condition to zero vertical velocity is imposed (gravity wave absorbing layers can be defined as well, but were not used for the Martian applications, though they will be considered for future improvements).

[11] In the horizontal dimension, the dynamical solver is available with three possible projections on the planetary sphere: Mercator (suitable for equatorial regions), Lambert Conformal (for midlatitudes), and Polar Stereographic (for high latitudes). Projections are defined by map scale factors, ensuring a regular computational grid whatever the map projection should be. Polar simulations are therefore devoid of any pole singularity, an usual drawback of the GCMs that requires the use of additional filtering. The spatial discretization is an Arakawa C grid, where normal velocities are staggered one-half grid length from the thermodynamic variables [*Arakawa*, 1966].

[12] In the temporal dimension, a third-order Runge-Kutta integration scheme is employed for improved numerical accu-

racy and stability: the maximum stable Courant Friedrichs Lewy (CFL) numbers for advection are increased by a factor of two compared to the regular leapfrog integration scheme [*Skamarock and Klemp*, 2008]. A time-splitting integration technique is implemented to prevent the meteorologically insignificant acoustic motions from triggering numerical instabilities [*Klemp et al.*, 2007]. Additional filters for acoustic external and internal modes damp residual instabilities possibly arising in the acoustic step integration.

[13] In the ARW-WRF Runge-Kutta time-integration scheme, while pressure gradient and divergence terms are simply second order and centered, spatial discretizations of the advection terms for momentum, scalars and geopotential are second through sixth order accurate [*Wicker and Skamarock*, 2002]. Martian simulations are performed with a fifth-order discretized advection. One peculiarity of the odd-order advection discretization is the inherent inclusion of a dissipation term [*Hundsdorfer*, 1995] with a coefficient proportional to the Courant number.

[14] However, as was pointed out by *Knievel et al.* [2007], this odd-ordered implicit scheme is not diffusive enough in low-wind or neutral/unstable stratification, and numerical noise in the wind fields might reach amplitudes comparable to the simulated winds. Such noise was found to be significant in the Martian case under near-surface afternoon superadiabatic conditions. The standard Martian simulations thus include the additional sixth-order diffusion scheme developed by *Knievel et al.* [2007], with a removal parameter set for Martian applications to 20% of the $2 \Delta x$ noise in one time step. While reducing the numerical noise near the surface to almost indiscernible amplitudes, the additional Knievel diffusion has little effect on the simulated meteorological fields.

[15] Particular adaptations were required to use the ARW-WRF dynamical solver in the Martian environment. Physical constants, such as the acceleration of gravity and the planetary rotation rate, were converted to the Martian values. Vegetation and ocean-related variables were not used, and replaced with variables more suitable for the Martian applications (e.g., thermal inertia). Martian dates are given by the aerocentric solar longitude L_s, which indicates the position of Mars with respect to the Sun (0, 90, 180, and 270 degrees are the beginning of the northern hemisphere spring, summer, fall, and winter, respectively). The terrestrial calendar was thus replaced with the LMD-GCM Martian calendar built on 669 Martian sols split in 12 "aerocentric longitude"-based months (each of them is $L_s = 30°$ long, and thus encloses an irregular number of Martian sols owing to the high eccentricity of the orbit), and 1 h was defined as 1/24 sol.

2.2. Martian Physics

[16] In any meteorological model, the 3-D dynamical core is coupled with parameterization schemes (most often 1-D) to compute at each grid point of the simulation domain the particular physics of the considered planetary environment: diabatic forcing of the atmospheric circulation (radiative transfer, soil thermal diffusion); sub-grid-scale dynamical parameterizations (Planetary Boundary Layer (PBL) diffusion and mixing, convective adjustment); tracer sources and sinks (microphysical processes, chemistry, dust sedimentation and lifting). The LMD-MGCM complete physical parameterizations are interfaced with the adapted ARW-WRF dynamical core, described in section 2.1, by a new

"driver" that is built on the same principles as the ARW-WRF terrestrial parameterization schemes, which are all switched off for the Martian applications. Thus, the LMD Martian Mesoscale Model shares the same comprehensive physical parameterizations as the LMD-MGCM, in order to simulate the Martian dust, CO_2, H_2O and photochemistry cycles [*Forget et al.*, 1999a; *Montmessin et al.*, 2004; *Lefèvre et al.*, 2004].

2.2.1. Physical Parameterizations

[17] The radiative transfer in the model accounts for CO_2 gas infrared absorption/emission [*Hourdin*, 1992] and visible and infrared dust absorption, emission and diffusion [*Forget*, 1998; *Forget et al.*, 1999a]. Description of the CO_2 condensation processes in the model is given by *Forget et al.* [1998]. Thermal conduction in the soil is simulated by the 11-layer soil model developed by *Hourdin et al.* [1993] for Mars (soil density and soil specific heat capacity are set as constants). Turbulent closure is based on turbulent viscosity with coefficients calculated from the "2.5-order" scheme by *Mellor and Yamada* [1982], improved by *Galperin et al.* [1988]. In the case where vertical mixing is handled in the independent 1-D physical packages, the native vertical mixing schemes in the ARW-WRF dynamical core are switched off, and the most appropriate choice for explicit horizontal diffusion is the built-in ARW-WRF scheme based on horizontal deformation [*Smagorinsky*, 1963].

[18] Recent improvements on the radiative transfer computations [*Dufresne et al.*, 2005], on the slope irradiance estimations [*Spiga and Forget*, 2008], on the dust lifting and sedimentation [*Forget et al.*, 1999b; *Newman et al.*, 2002], on the water cycle and water ice clouds [*Montmessin et al.*, 2004], and on the photochemical species [*Lefèvre et al.*, 2004], particularly ozone [*Lefèvre et al.*, 2008], are also natively included in the LMD Martian Mesoscale Model. The nonlocal thermodynamic equilibrium (NLTE) parameterizations for thermosphere applications [*González-Galindo et al.*, 2005] as well as estimations of the atmospheric exchanges with the Martian regolith [*Böttger et al.*, 2005], are also available in the model, albeit not activated in the present simulations.

[19] Upcoming improvements of the LMD-MGCM physics [*Forget et al.*, 2007], following the recent measurements by instruments on board Mars Express (MEx) and MRO, will be included in the LMD Martian Mesoscale Model too. Examples of future parameterizations that will be added in both models are the radiative effects of water ice clouds, which could significantly modify the atmospheric temperatures [*Wilson et al.*, 2007], and the new dust radiative properties derived from recent measurements by the OMEGA instrument on board MEx (A. Määttänen et al., A study of the properties of a local dust storm with Mars Express OMEGA and PFS data, submitted to *Icarus*, 2008) and the CRISM instrument on board MRO (M. J. Wolff and M. Vincendon, personal communication, 2008).

[20] Two physical parameterizations of the LMD-MGCM, specifically designed for synoptic-scale meteorological applications, are not used in the mesoscale applications.

[21] First, in the mesoscale domain, the topographical field is described with horizontal resolutions from tens of kilometers to hundreds of meters. The *Lott and Miller* [1997] sub-grid-scale topographical drag parameterization and the *Miller et al.* [1989] gravity-wave drag scheme can thus be switched

off, as the topographical influence on the atmospheric flow is computed by the dynamical core at the chosen mesoscale resolutions.

[22] Second, in order to ensure numerical stability, and to account for sub-grid-scale mixing processes insufficiently handled in the PBL scheme, it is usually necessary to modify any unstable layer with negative potential temperature gradients (an usual near-surface situation during Martian afternoons) into a neutral equivalent [*Hourdin et al.*, 1993]. As pointed out by *Rafkin* [2003], the use of such an artificial convective adjustment scheme might be questionable in Martian atmospheric models, should they be GCMs or mesoscale models. Since numerical stability is ensured in the LMD Martian Mesoscale Model by choosing the appropriate dynamical time step with respect to the CFL condition, and using the aforementioned ARW-WRF nominal filters and diffusion schemes, the convective adjustment scheme used in the LMD-MGCM can thus be switched off in the LMD Martian Mesoscale Model. We provide additional clues for this choice in section 3.2.

2.2.2. Physical Time Step

[23] Invoking physical packages often with respect to the dynamical computations was found to be necessary to accurately account for near-surface friction effects where the wind acceleration is particularly high, typically in regions of strong Martian topographically driven circulation. In such areas, if the ratio between the physical time step and the dynamical time step is above ~5, the model predicts winds spuriously increasing with the chosen ratio and varying with the horizontal resolution. On the contrary, if this ratio is less than ~5, the simulated winds neither vary significantly with the chosen ratio nor with the horizontal resolution.

[24] A ratio equal to 1 is chosen in the standard LMD Martian Mesoscale Model simulations performed in this paper. This choice is in conformity with the strategy adopted in the terrestrial ARW-WRF model. Besides, computing the physical parameterizations at the same frequency as the dynamical integration is profitable to some physical parameterizations, such as the formation of clouds (which is sensitive to rapid temperature change). Note that radiative transfer computations are carried out less often to save computational time.

[25] When the ratio between the physical time step and the dynamical time step is superior to 1, two distinct strategies could be adopted. Interestingly, we found that splitting the physical tendency in equal parts and blending it with the dynamical tendency at each dynamical time step computation is slightly more stable (understand: allows for higher dynamical time steps) than applying the whole physical tendency when the physical parameterizations are computed, and letting the dynamical core naturally evolve until the next physics call. However, an analysis of the simulated meteorological fields in both cases does not reveal significant differences.

2.3. Initial and Boundary Conditions
2.3.1. Starting State and Horizontal Boundaries

[26] Mesoscale simulations can be performed in a limited domain anywhere on the planet. Thus, boundary conditions for the main meteorological fields (horizontal winds, temperature, tracers) have to be provided during the simulations, in addition to an atmospheric starting state. Idealized simu-

lations usually require the use of periodic, symmetric or open boundary conditions, whereas real-case simulations need specified climatologies at the boundaries.

[27] The specified boundary conditions and the atmospheric starting state are derived from previously performed $64 \times 48 \times 25$ (i.e., horizontal resolution of $5.625°$ in longitude and $3.75°$ in latitude, model top ~80 km altitude) LMD-MGCM simulations which have reached equilibrium, typically after ~10 simulated years. In this paper, GCM results are used every Martian hour to constrain the mesoscale model at the domain boundaries. Temporal interpolations to each mesoscale time step and spatial interpolations on the mesoscale domain are performed from the LMD-MGCM inputs. A relaxation zone of a given width (user-defined, usually 5 grid points) is implemented at the boundaries of the ARW-WRF domain to enable both the influence of the large-scale fields on the limited area, and the development of the specific mesoscale circulation inside the domain. The interpolations and the use of a relaxation zone prevent the prescribed meteorological fields at the lateral boundaries from having sharp gradients and from triggering spurious waves or numerical instabilities (the situation where the relaxation zone crosses steep topographical gradients should, however, be avoided).

2.3.2. Nesting or Single-Domain Strategy?

[28] The model includes one-way and two-way (or "feedback") nesting capabilities. The nested simulations feature two kinds of domains where the meteorological fields are computed: the "parent" domain, with a large geographical extent, a coarse grid resolution, and specified boundary conditions, and the "nested" domains, centered in a particular zone of interest, with a finer grid resolution, and boundary conditions provided by its parent domain.

[29] In the present study, the nesting capabilities were used only if deemed necessary, and single-domain simulations were the primary type of run performed.

[30] First, employing the same physical parameterizations in the mesoscale model computations and in the GCM simulations defining the boundary and initial conditions, ensures a very consistent meteorological forcing at the boundaries of the mesoscale domain. This assumption was not denied by further examination of the performed simulations: mesoscale predictions are not unrealistically departing from the LMD-MGCM prescribed fields at the boundaries, and the mesoscale influence naturally adds to the synoptic (large-scale) tendency communicated at the boundaries.

[31] Second, the single-domain approach is appropriate as long as the variations of near-surface winds, pressure and temperature induced by "passing" thermal tides through the east-west boundaries are not unrealistic. This criterion is specific to Martian mesoscale modeling and was described by *Tyler et al.* [2002]. In the various simulations performed with the LMD Martian Mesoscale Model, a likely spurious influence of the passing thermal tides was only detected in the near-surface meteorological fields calculated at the ~5 near-boundaries grid points. The amplitudes of the departures were negligible ($\delta T \lesssim 3$ K; δu, $\delta v \lesssim 5\%$) and did not require the use of domains nested inside one semihemispheric parent domain [*Tyler et al.*, 2002]. However, the analysis of the simulated fields at the near-boundaries grid points should be carried out with caution when choosing the single-domain approach. A practical solution to this drawback is to define a

Table 1. Simulation Settings[a]

	xyz Grid	Δx (km)	Δz[b] (m)	π_t[c] (Pa)	Δt (s)	L_s (deg)	Plot[d]	Comments
GCM-like	74 × 50 × 26	~300[e] (5°)	2200	1	185[f]	0, 180, 270	7th	hydrostatic option; periodic x boundary; water cycle on
Chryse Planitia (40°W, 32°S)	181 × 181 × 61	20	670	5	25	150	2nd–5th	1st level ~0.6 m ABG
Valles Marineris (68°W, 8°S)	401 × 121 × 61	12	700	3	10	320	4th	
Gusev (175.4°E, 14.5°S)	150 × 150 × 71	0.1 (LES)	140	250	1/2	2.5	1st	periodic x boundary; periodic y boundary; uniform initial state[g], zero initial winds
Tharsis (120°E, 5°N)	200 × 200 × 61	20	700	3	20	90, 120	4th	water cycle on (new TES reference),
+ Arsia Mons Nest (120.5°E, 9.7°S)	205 × 205 × 61	5	700	3	10	120	4th	1-way nesting
Olympus (134°E, 18°N)	201 × 201 × 61	10	700	3		175	6th	fixed thermal inertia 85 J m^{-2} K^{-1} s$^{-0.5}$

[a]All other settings (filters, physical packages) are standard, as indicated in the paper.

[b]Any vertical level repartition can be chosen in the ARW dynamical core; we chose to define levels equally spaced in altitude. However, to correctly resolve the boundary layer, the first eight levels are fixed to the values $\eta = 1, 0.9995, 0.998, 0.995, 0.985, 0.97, 0.94$, and 0.9, which correspond (roughly) to layers' altitudes above ground of 3, 14, 38, 112, 260, 535, 975, and 1600 m. If the model top is rather low (e.g., LES studies), only the first four or five values are fixed.

[c]Except for LES studies, the model top should be chosen at the summit of Martian tropopause (around 3 Pa) where isothermal temperature structure is observed [Tyler et al., 2002].

[d]Indicates the sol chosen for analysis in this paper. Usually, the spin-up time is ~1 sol. When the water cycle is computed, a longer spin-up time can be expected (about 2 sols).

[e]The ARW dynamical core does not enable the definition of the lat-lon projection usually employed in the GCMs (at least in version 2.2 used for the present Martian applications). Mercator projection is chosen instead. Consequently, the indicated value for Δx is correct for the longitude coordinates, but only indicates the maximal value of horizontal resolution for the latitude coordinates (poleward decrease due to the Mercator projection).

[f]Interestingly, this value is higher than the LMD-MGCM dynamical time step of 92.5 s; this is a direct consequence of the Runge-Kutta stability improvements in the ARW dynamical core.

[g]The terrain properties for this simulation are typical of the Gusev site: elevation, −1905 m; thermal inertia, 231 J m^{-2} K^{-1} s$^{-0.5}$; albedo, 0.23; dust opacity, 0.3.

large domain, centered on the chosen area of interest, with a sufficient number of grid points (75 × 75 being a minimal requirement).

[32] Third, *Dimitrijevic and Laprise* [2005] showed, by the so-called "Big Brother" approach, that the single-domain approach yields unbiased results when the boundary forcing involves a minimum of ∼8–10 GCM grid points. Thus, given the resolution of the GCM fields used in this study to constrain the LMD Martian Mesoscale Model, single-domain simulations with, for instance, a horizontal resolution of 20 km shall be performed on at least 133 × 88 grid points. *Antic et al.* [2006] found that the "8–10 grid points" limit can be lowered in situations of complex topography, because the dynamical influence of these mesoscale features is responsible for the larger part of the mesoscale circulation in the domain. Such situations are rather common on Mars, and the aforementioned "minimal" grid can be of slightly smaller horizontal extent in areas such as Olympus Mons or Valles Marineris.

[33] Table 1 summarizes the settings of all the simulations performed in this study: one shall note that the sizes of the simulation grids were chosen in order to ensure the applicability of the single-domain approach. The nesting technique is used only when defining a single domain with sufficient geographical extent would have required too many grid points to handle the computations within reasonable CPU time. For instance, with "64 × 48" GCM simulations as boundary conditions, the use of the single-domain strategy to model the Arsia Mons circulation at 5 km resolution imposes a simulation grid of at least 531 × 354 points. As is stated in Table 1, the nesting technique is employed for this kind of simulation. While the use of two to five nests is adopted in most of the existing Martian mesoscale models, the strategy retained in the present paper relates to most terrestrial studies [e.g., *Plougonven et al.*, 2008], in which horizontal resolutions range from ∼50 km to 15 km in the parent (or single) domain and from ∼10 km to 3 km in one nested domain, with 100 to 200 grid points for each horizontal dimension.

2.3.3. Surface Fields

[34] Surface static data intended for the mesoscale domain are extracted from maps derived from recent spacecraft measurements: 64 pixel-per-degree (ppd) MOLA topography [*Smith et al.*, 2001], 8 ppd MGS/Thermal Emission Spectrometer (TES) albedo [*Christensen et al.*, 2001], 20 ppd TES thermal inertia [*Putzig and Mellon*, 2007]. A smoother composite thermal inertia map derived from *Palluconi and Kieffer* [1981], *Mellon et al.* [2000] and *Vasavada et al.* [2000] can be alternatively used for better continuity with LMD-MGCM simulations. Except for CO_2 ice covered areas, emissivity is set to 0.95. The roughness length z_0 is set to the constant value of 1 cm, but further versions of the model will use spatially varying z_0 [*Hébrard et al.*, 2007]. Initial values for time-varying surface data, such as CO_2 and H_2O ice on the surface and soil temperatures, are derived from the GCM simulations. The latter initialization reduces the spin-up time for surface temperature to roughly one simulated sol.

[35] The LMD Martian Mesoscale Model has the complete ability to simulate the dust cycle (lifting, sedimentation, transport). However, the high sensitivity of the results to the assumptions made on threshold wind stress and injection

rate [*Basu et al.*, 2004] leads us to postpone these issues to future studies. Instead, similarly to the reference LMD-MGCM simulations, dust opacities are prescribed in the mesoscale model from 1999–2001 TES measurements, thought to be representative of Martian atmospheric conditions outside of planet-encircling dust storm events [*Montabone et al.*, 2006]. In the vertical dimension, as described by *Forget et al.* [1999a], and in accordance with the general consensus of well-mixed dust in equilibrium with sedimentation and mixing processes [*Conrath*, 1975], dust mixing ratio is kept constant from the surface up to a given elevation z_{max} above which it rapidly declines. Both in the nominal GCM and mesoscale simulations, z_{max} as a function of areocentric longitude and latitude is calculated from the "MGS scenario" [*Forget et al.*, 2003].

2.3.4. Vertical Interpolation

[36] In the process of initialization and definition of boundary conditions, the vertical interpolation of GCM meteorological fields to the terrain-following mesoscale levels must be treated with caution. While deriving the near-surface meteorological fields from GCM inputs, one may address the problem of underlying topographical structures at fine mesoscale horizontal resolution, e.g., a deep crater that is not resolved in the coarse GCM case.

[37] A crude extrapolation of the near-surface GCM fields to the mesoscale levels is usually acceptable for terrestrial applications. On Mars, owing to the low density and heat capacity of the Martian atmosphere, the surface temperature is to first order controlled by radiative equilibrium, and thus it is left relatively unaffected by variations of topography [e.g., *Nayvelt et al.*, 1997]. A practical consequence, which renders an extrapolation strategy particularly wrong on Mars, is that the near-surface temperature and wind fields vary much more with the distance from the surface than with the absolute altitude above the areoid (or equivalently with the pressure level). Initial tests carried out with the extrapolation strategy showed that differences between temperatures at the boundaries and temperatures computed within the mesoscale domain close to these boundaries often reach 20–30 K near the surface. An interpolation based only on terrain-following principles solves this problem near the surface but was found to lead to numerical instabilities at higher altitudes during the mesoscale integrations.

[38] Therefore, input meteorological data need to be recast on intermediate pressure levels P' with a low-level smooth transition from terrain-following levels (for the near-surface environment) to constant pressure levels (for the free atmosphere at higher altitude). We thus have $P'(x, y) = \alpha + \beta P_s(x, y)$, P_s being the surface pressure at the resolution of the GCM simulations. To ensure a realistic low-level transition, the technique described by *Millour et al.* [2008], based on high-resolution GCM results, is employed to calculate the P' levels. The mesoscale surface pressure field p_s is an input parameter of the method, since the near-surface adiabatic cooling over mountains and warming within craters are taken into account. Note that $p_s(x, y)$ is calculated from $P_s(x, y)$ on the basis of the high-resolution topography of the mesoscale domain $z(x, y)$ by

$$p_s(x,y) = P_s(x,y)\, e^{\frac{g\,[Z(x,y)-z(x,y)]}{R\,T(x,y)}}$$

where $Z(x, y)$ is the topography at the resolution of the GCM simulations, R the gas law constant, g the acceleration of gravity, and $T(x, y)$ the temperature predicted by the GCM 1 km above the surface [see *Spiga et al.*, 2007]. Without reinterpolating the data, the intermediate pressure P' levels are then simply converted into their mesoscale counterparts p' by substituting p_s for P_s in the formula $P'(x, y) = \alpha + \beta P_s(x, y)$. Finally, the built-in ARW-WRF vertical interpolation onto the final mesoscale terrain-following levels can be performed, as the problem of extrapolation is solved by the use of the intermediate pressure levels p'.

[39] The initial atmospheric state obtained through this "hybrid" method ensures low-amplitude adjustments of the meteorological fields by the mesoscale model at the beginning of the performed simulations (i.e., in the first thousands of seconds). Furthermore, the continuity between the large-scale forcing and the mesoscale computations near the limits of the domain, as well as the numerical stability of the simulations, appear as significantly improved compared to methods either based on extrapolation (especially in areas of uneven terrains) or terrain-following interpolation.

3. Simulations

[40] The purpose of the case studies in this paper is to validate the LMD Martian Mesoscale Model upon well-constrained GCM simulations, lander measurements, and independent robust mesoscale modeling studies. The characteristics of the presented simulations are summarized in Table 1. The performance of the model is investigated at various horizontal scales, including synoptic scales, mesoscales and microscales. At the same time, the performed simulations give insights into the various mesoscale and microscale meteorological phenomena on Mars.

3.1. Large-Scale Simulations

[41] Even if mesoscale models are specifically designed for regional meteorology, they can also be used as GCMs after a few adaptations [*Richardson et al.*, 2007]. The goal of this section is not to address any synoptic-scale meteorological issue, but to check the performance of the ARW-WRF dynamical core with all the realistic Martian atmospheric forcings provided by the LMD Martian physics. Since the LMD-MGCM and the LMD Martian Mesoscale Model share the same physical parameterizations, comparing the diagnostics of the two models is an efficient test of the dynamical core itself. Besides, as the LMD-MGCM fields are used as boundary conditions for mesoscale applications, performing such a check of consistency is a necessary preliminary step.

[42] The LMD-MGCM simulations that are used as a reference in this section are of slightly higher resolution in longitude (5°) than the ones used for the standard mesoscale initializations. As reported in Table 1, the mesoscale "GCM-like" domain is defined with the same resolution of 5° in longitude. For the sake of comparison, unlike the standard LMD Martian Mesoscale Model simulations performed in this paper at finer resolutions, the convective adjustment and the gravity-wave drag schemes are included, and hydrostatic equilibrium is assumed. The domain is global in the longitude dimension, with east-west periodic boundary conditions to mimic the behavior of a GCM. The evolution of the meso-

scale model in the longitudinal dimension is consequently free of any external constraints.

[43] Northern and southern boundary conditions are prescribed at latitudes ±75° with a relaxation zone extending to latitudes ±69°. Thus, we chose to limit the rigorous comparison between the two models to latitudes below ±60°. Another reason for this is the choice of the Mercator projection in the "GCM-like" mesoscale simulation, which is not fully appropriate for modeling the atmospheric circulation in the high latitudes.

[44] First of all, the surface temperature cycle and the radiative fluxes were checked to be similar in the mesoscale "GCM-like" simulations and the GCM simulations. Then, the major atmospheric structure was examined after seven sols of simulation for three typical seasons (northern fall, northern winter, and northern spring). Results are shown in Figure 1.

[45] The overall thermal atmospheric structure is well reproduced by the LMD Martian Mesoscale Model at these three seasons, as could be inferred from the potential temperature field. Vertical profiles of temperature at various locations on Mars (not shown) also compare closely between both simulations, except in the topmost five levels. The atmospheric structure simulated by the mesoscale model is thus consistent with the LMD-MGCM simulated thermal structure, which was validated against the available data from spacecraft measurements (mostly MGS TES and radio-occultation temperature measurements) [*Millour et al.*, 2008]. Correct reproduction of the zonal jets is then expected from the thermal wind balance, once the thermal structure is validated [*Lewis and Read*, 2003]. The fall and spring symmetrical jets and winter hemisphere jet are indeed predicted by the mesoscale model, in qualitative and quantitative agreement with the results of the LMD-MGCM. As a complement, it is worth mentioning the similarity between the western boundary current on the Tharsis flanks [*Joshi et al.*, 1995] simulated by the LMD Martian Mesoscale Model and by the LMD-MGCM (figure not shown).

[46] Differences can, however, be observed between the two models. First, they disagree close to the top of the mesoscale domain. There may be two reasons for this: (1) Artificially prescribing a fixed top at a given pressure level could be the source of unrealistic computations (as could be observed in the top five levels that were removed from Figure 1 for the sake of clarity). (2) The Martian Hadley cell could extend up to 60 km, especially during the solstices; prescribing a model top around 41 km clearly prevents the representation of the meridional transport of momentum and heat from being fully accurate [*Wilson*, 1997; *Forget et al.*, 1999a; *Toigo and Richardson*, 2002].

[47] Second, differences are significant in the northern polar night at higher altitudes. The polar night is an environment driven by dynamical processes rather than radiative processes, revealing the subtle differences between the various dynamical cores and their related assumptions. Therefore, although the LMD-MGCM and LMD Martian Mesoscale Model share similar physical parameterizations, the two models might yield different diagnostics in the polar night, as is the case between the finite difference LMD-MGCM and the spectral Oxford Mars GCM (L. Montabone, personal communication, 2007) [see also *Giuranna et al.*, 2008]. In addition to the influence of the chosen numerical method to integrate the dynamical equations, the diagnostics derived from the models are sensitive to the dynamical filtering used in the polar regions to overcome the pole singularity problem. In particular, the fact that dynamical filtering is performed at high latitudes in the LMD-MGCM and not in the LMD Martian Mesoscale Model may explain the significant differences between both models in the polar night. Besides, the observed differences could be due to the different map projections at high latitudes. The limited vertical extent of the Hadley cell in the mesoscale model, owing to the low model top, may also explain the departures between both models (e.g., zonal means of temperature differences can reach ∼10 K) in regions where the descending branch of the Hadley cell is known to induce strong polar warming [*Wilson*, 1997].

[48] Since water ice clouds have a nonlinear dependence with temperature, and water vapor atmospheric repartitioning is strongly influenced by the synoptic meridional transport [*Montmessin et al.*, 2004], slight wind or temperature departures between the LMD Martian Mesoscale Model and the LMD-MGCM can lead to significant water vapor differences, but at the same time providing interesting insights on the main contrasts. For instance, differences in the meridional transport, induced by the finite model height, can be observed around 20–25 km altitude near the equator during the three seasons. The lack of transport efficiency of the Hadley cell can also be identified around 50° latitude in the northern winter hemisphere, where the polar warming was found previously to be diversely simulated in both models. Finally, the near-surface differences at northern fall around 50°S and northern spring around 50°N are probably due to the differences of grid point positions between the two models, which might influence the edge of the retreating seasonal polar caps, and thus the associated water vapor release into the atmosphere.

[49] To summarize, despite departures that could be accounted for by the structural differences between the GCM and the mesoscale model, the vertical and latitudinal synoptic structure is reasonably reproduced by the mesoscale model.

[50] The behavior in the freely evolving longitudinal dimension (thanks to the use of periodic boundary conditions) has to be investigated as well. Analyzing the tidal structure is a suitable test for this purpose, and more generally, enables one to test the dynamical core performance.

Figure 1. Comparisons between the 7th day of simulation of the LMD Martian Mesoscale Model in "GCM-like" mode and the LMD Martian GCM reference. The zonal mean of the magnitude of the difference between the mesoscale model and the GCM is shaded for three fields: (top) potential temperature, (middle) zonal wind, and (bottom) water vapor mixing ratio. The contours of the zonal mean of the corresponding fields simulated by the LMD Martian Mesoscale Model are superimposed. Three different seasons are considered: (left) northern fall ($L_s = 180°$), (middle) northern winter ($L_s = 270°$), and (right) northern spring ($L_s = 0°$). Note that contrary to the "Tharsis clouds" simulation, the water cycle is set here to reproduce the "old" TES reference, wetter than the "new" reference [*Smith*, 2008].
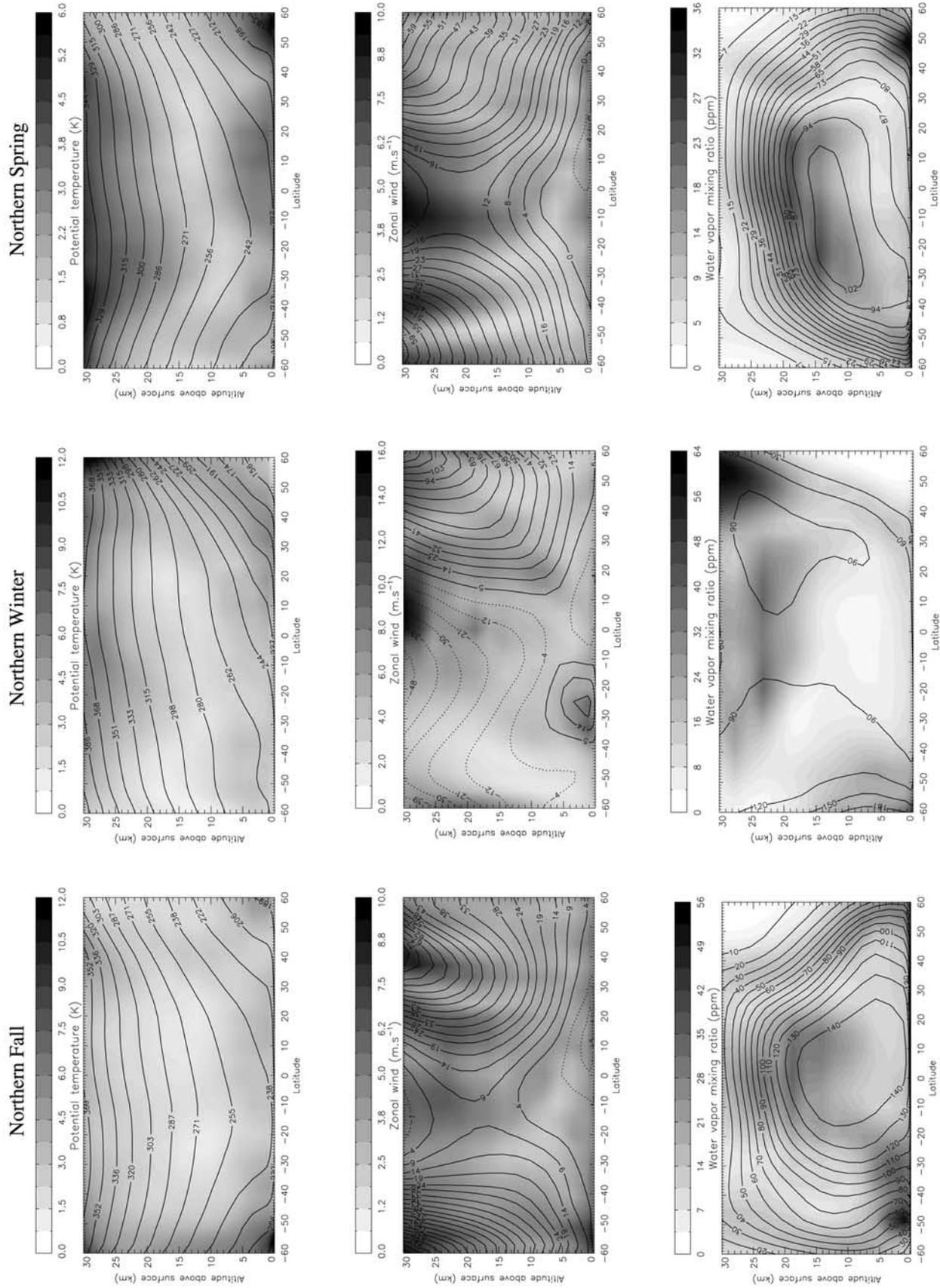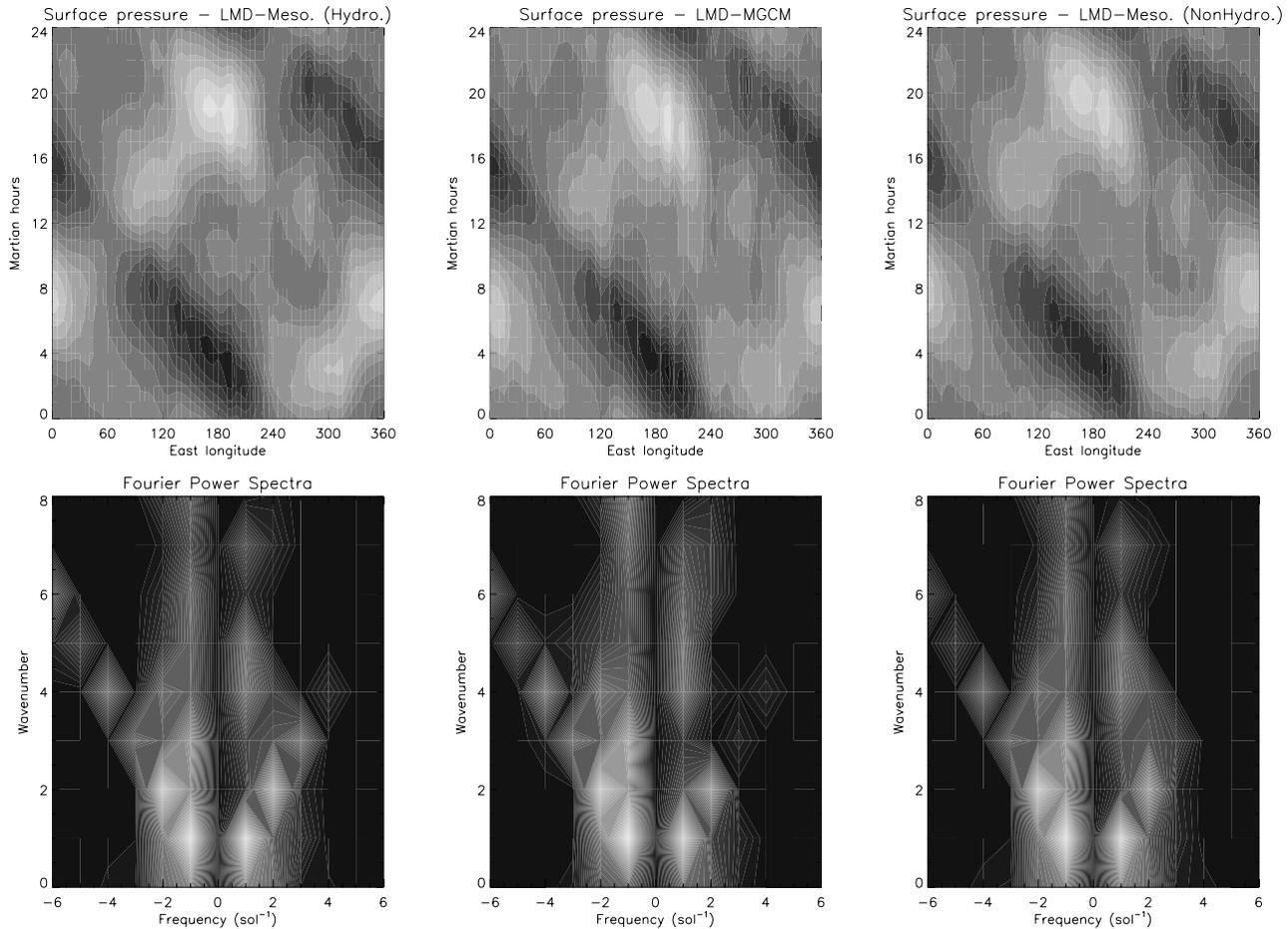
Figure 1

Figure 2. (top) Hovmöller plot of the equatorial surface pressure anomalies p_s for the 7th day of simulation. The average surface pressure value for each sol is subtracted from the raw equatorial surface pressure signal, which removes the topographical permanent component. Maximum anomalies are ±35 Pa. Results from (middle) the reference LMD Martian GCM are compared to the LMD Martian Mesoscale Model diagnostics, obtained by (left) hydrostatic and (right) nonhydrostatic "GCM-like" simulations with cyclic longitudinal dimension. The same black and white scale is employed in both plots. (bottom) Representation of the equatorial surface pressure anomalies in the spectral space by Fast Fourier Transformation. The plotted quantity is the logarithmic power spectra $\log_{10}(\tilde{p}_s^2)$. Black is used for values below -2.5; white corresponds to values of 1.5 (the same black and white scale is employed in both plots). Westward diurnal and eastward Kelvin modes can be clearly identified, with associated harmonics. Note the various diagnostics for the amplitude of the Kelvin wave number 3 mode (a point which seems rather difficult to explain).

Wave analysis is carried out using the surface pressure signal at the equator during the northern winter, where the atmospheric response to solar heating is particularly strong owing to increased dust loading [e.g., *Read and Lewis*, 2004]. As could be concluded from Figure 2, the tidal power spectra obtained with the two models closely match. The Sun-synchronous diurnal and semidiurnal modes (westward propagating) are reasonably reproduced in the LMD Martian Mesoscale Model, as well as the diurnal Kelvin mode (eastward propagating). Higher-frequency modes, of lesser amplitude, are also present in the resolved spectra.

[51] An intercomparison of Martian mesoscale models carried out in 2003 revealed an overestimation of the diurnal surface pressure cycle predicted by the nonhydrostatic models, compared to the results of hydrostatic models [*Tyler and Barnes*, 2005]. The source of the problem was the diabatic heating terms in the pressure tendency equation being neglected in the nonhydrostatic dynamical cores (namely, RAMS and MM5 [see, e.g., *Dudhia*, 1993]) used for the Martian applications. This approximation yields negligible differences with the fully compressible calculations on Earth, but not on Mars, leading to the aforementioned overestimation of the thermal tides signatures.

[52] One of the improvements of the new ARW-WRF mesoscale model, compared to its predecessor MM5, is the integration of the fully compressible equations: the pressure tendency equation is replaced by the equivalent, though much simpler, geopotential equation in which the diabatic heating is included [see *Laprise*, 1992, equations (39) and (39')]. The LMD Martian Mesoscale Model is thus devoid of the problem that was identified in earlier Martian mesoscale models (and corrected since then). To confirm this statement,

"GCM-like" simulations in full nonhydrostatic mode were carried out with the LMD Martian Mesoscale Model: it was found that the amplitudes of tidal and Kelvin modes in the surface pressure signal are comparable to the hydrostatic estimates (see Figure 2). The only significant differences ($\sim 3-4$ Pa) are related to the wave number 3 Kelvin mode, but the amplitude of this mode also differs between the mesoscale simulations in hydrostatic mode and the GCM estimates.

[53] The consistent reproduction of the baroclinic waves in the LMD Martian Mesoscale Model was also checked. Though the structure and the amplitude of these waves are similar in the mesoscale and the LMD-MGCM simulations (figures not shown), the phasing of the typical high- and low-pressure features varies between both models. Such differences could be expected from the absence of longitudinal forcing in the mesoscale simulations and the distinct map projection in the two models, yielding different horizontal resolutions at midlatitudes.

3.2. Viking and Pathfinder Landing Sites

[54] Martian in situ meteorological measurements are particularly sparse. Near-surface measurements performed by the Viking (VL) and the Mars Pathfinder (MPF) Landers can, however, provide some "ground truth" for the mesoscale models to compare to. Such a comparison is possible owing to the high repeatability of the Martian climatic system, which is mostly controlled by local time and season, with a generally low interannual variability only disturbed by the occurrence of dust storms. A strong limitation of the validation of the mesoscale model diagnostics against lander data is the fact that the measurements were made on relatively flat terrain, whereas most of the interest for near-surface mesoscale phenomena resides in topographically uneven areas.

[55] In this section, the Viking Lander 2 observational data are not used to help validate the LMD Mesoscale Model. *Toigo and Richardson* [2002] carried out detailed and instructive comparisons between their mesoscale simulations and the VL2 measurements, but the agreement was less favorable than the VL1 and Pathfinder cases, owing to the combination of strong day-to-day variability with complex interactions between tidal and slope forcings at the Viking Lander 2 site. On the contrary, the validation of the *Tyler et al.* [2002] mesoscale model was not based on the VL2 data. The authors chose instead to focus on the analysis of the diurnal cycles in a mesoscale domain enclosing both VL1 and Pathfinder sites; we adopted a similar approach in this paper.

[56] As indicated in Table 1, the latitude-longitude extent of our second simulation domain is roughly [2°W–80°W] × [2°N–58°N]. The whole Chryse Planitia region, including both the VL1 and the MPF landing sites, is thus covered, at enough distance from the boundaries where the LMD-MGCM meteorological inputs are defined. Figures 3 and 4 summarize the results at the VL1 and Pathfinder landing sites. The overall reproduction of the near-surface temperature, surface pressure and wind diurnal cycles by the LMD Martian Mesoscale Model is satisfying.

[57] The simulations were performed with and without the convective adjustment, to assess the influence on the near-surface meteorological fields of this somewhat artificial adjustment to neutral conditions. Convective adjustment is responsible for the "sharkfin appearance" (to quote *Rafkin*

et al. [2001]) of the afternoon variations of the near-surface temperature in Figures 3 and 4. Results are rather similar with the first level in the LMD Martian Mesoscale Model at 1 m (shown) or 5 m (not shown) above the surface. On the contrary, when the convective adjustment is removed, and the superadiabatic layer is set free to develop during the afternoon, the modeled variations of the near-surface temperature with the local time are more consistent with the observed variations.

[58] Without convective adjustment, the temperature is overestimated by $\sim 5-10$ K during the afternoon, compared to the VL1 and Pathfinder measurements. Late afternoon and evening temperatures are also overestimated, which could be an effect of thermal inertia values higher than in reality. It should be kept in mind that the near-surface temperature is very sensitive to the assumptions made for the soil thermal inertia and albedo properties, as well as the dust concentration in the atmosphere. As a consequence, the independent models of *Rafkin et al.* [2001], *Tyler et al.* [2002], and *Toigo and Richardson* [2002] yielded different quantitative results with underestimation/overestimation in the range [−10 K, 10 K]. The afternoon overestimation in our model is within this uncertainty range.

[59] Turning the convective adjustment on and off does not produce much impact on the surface pressure cycle (Figures 3 and 4) and wind daily rotation (Figure 4), which are correctly accounted for in the LMD Martian Mesoscale Model compared to the data. The maximum surface pressure in the morning is not well reproduced by the mesoscale model, for reasons difficult to evaluate. This difficulty was similarly found in the hydrostatic mesoscale simulations by *Tyler et al.* [2002] and LMD-MGCM simulations. In addition, one may observe a delay (also noticed by *Tyler et al.* [2002]) in the evening wind overturning compared to the measurements.

[60] The influence of the convective adjustment on the near-surface mesoscale meteorology can be clearly seen from the simulated wind speeds, as a result of the aforementioned significant differences on the temperature structure. While the mean wind velocity could be approximatively replicated by the model should the convective adjustment be on or off, the maximal variability during the afternoon revealed by the Viking measurements is absent from the convective adjustment simulations, but clearly established in the "no convective adjustment" simulations.

[61] Winds measured by Pathfinder are unfortunately not reliable, especially in the afternoon where the error might exceed 30% (J. Murphy, personal communication and data delivery, 2008). It is, however, possible to keep only the wind speeds consistently retrieved by both Pathfinder sensors (difference between measured values below 10%) to identify maximal wind values of ~ 20 m s^{-1} and frequent gusts between 10 and 15 m s^{-1}. With convective adjustment, the mesoscale maximal winds in the afternoon are 5–6 m s^{-1}, whereas the values are 8–10 m s^{-1} when no convective adjustment is employed, which allows us to draw the same conclusion as the VL1 comparison (the most powerful gusts identified in the Pathfinder data cannot be reproduced by the mesoscale model at the resolution chosen for the Chryse Planitia simulation and would require finer resolution simulations).

[62] Thus, the observed near-surface gustiness of the Martian atmosphere is reproduced with improved accuracy
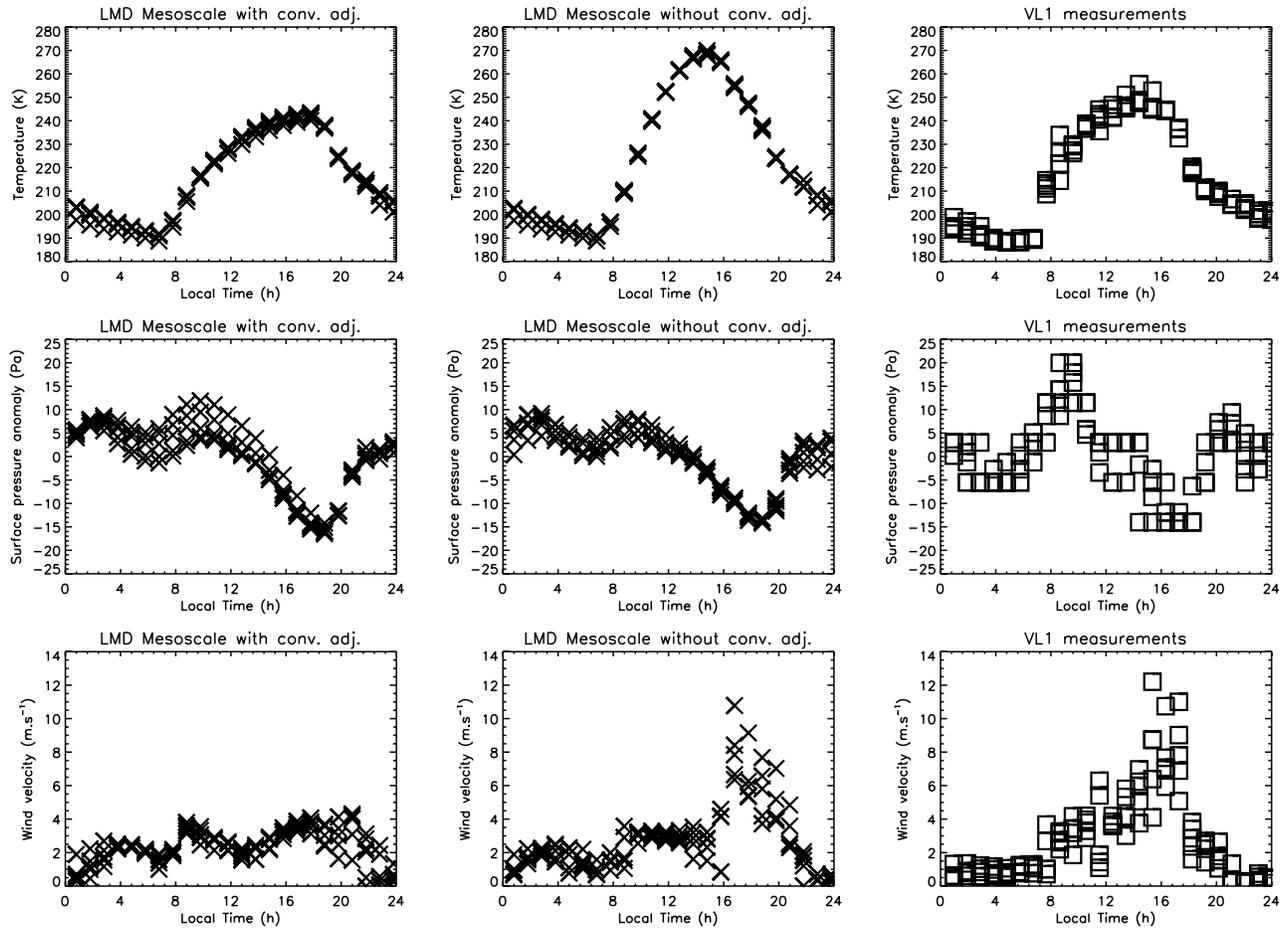
Figure 3. Comparison of the meteorological fields predicted by the mesoscale model (grid point coordinates 48.09°W, 22.24°N) with Viking Lander 1 measurements (coordinates 47.95°W, 22.27°N). The first level of the model is ~0.6 m above the surface, and the second level is ~3.5 m. Temperature values 1.6 m above the surface (altitude of the Viking Lander 1 sensor) are obtained by linear interpolation in the vertical dimension. Wind values 1.6 m above the surface are derived from the simulated values assuming a logarithmic wind profile with surface roughness of 1 cm. Surface pressure anomalies are computed using a daily average value. Mesoscale model results with and without convective adjustment are shown.

by the mesoscale model if we let the model naturally evolve under superadiabatic afternoon conditions, instead of artificially stabilizing the temperature profile with the convective adjustment scheme. The comparison with lander measurements confirms that if ever needed, the convective adjustment schemes implemented in most Martian GCMs are probably simplistic and in need for further improvements.

3.3. Valles Marineris Winds

[63] Near the surface, nighttime cooling and daytime warming impose terrain-following behavior of the atmospheric density. As a result, according to the Bjerknes circulation theorem, topographical slopes induce significant baroclinic production $\nabla \rho \times \nabla p$, which results in afternoon anabatic (upslope) and nighttime katabatic (downslope) atmospheric motions. Owing to the short radiative time scales and low thermal inertia of the Martian atmosphere, amplitudes of the slope winds on Mars are 2 to 3 times higher than their terrestrial counterparts [*Gierasch and Sagan*, 1971; *Ye et al.*, 1990].

[64] As some of the steepest slopes on Mars can be found in the Valles Marineris canyon, dramatic thermally driven near-surface winds might develop in this area, arousing the interest of Martian mesoscale modelers. Since winds have never been measured in the vicinity of the Valles Marineris canyon, results from the mesoscale models are the only available meteorological diagnostics in this region. The Valles Marineris case study was thus a preferential target of the aforementioned studies involving 3-D mesoscale modeling, providing another reference upon which the performance of the present model can be assessed.

[65] The overall structure of the slope winds system around Valles Marineris is basically the same in the four independent studies by *Tyler et al.* [2002], *Toigo and Richardson* [2003], *Rafkin and Michaels* [2003], *Richardson et al.* [2007]. Strong afternoon canyon outflow results from upslope winds, while during the night, winds reverse to downslope directions, inducing an inflow into the canyon. As can be seen in Figure 5, these main characteristics are reproduced by the LMD Martian Mesoscale Model. No underlying contours are necessary to
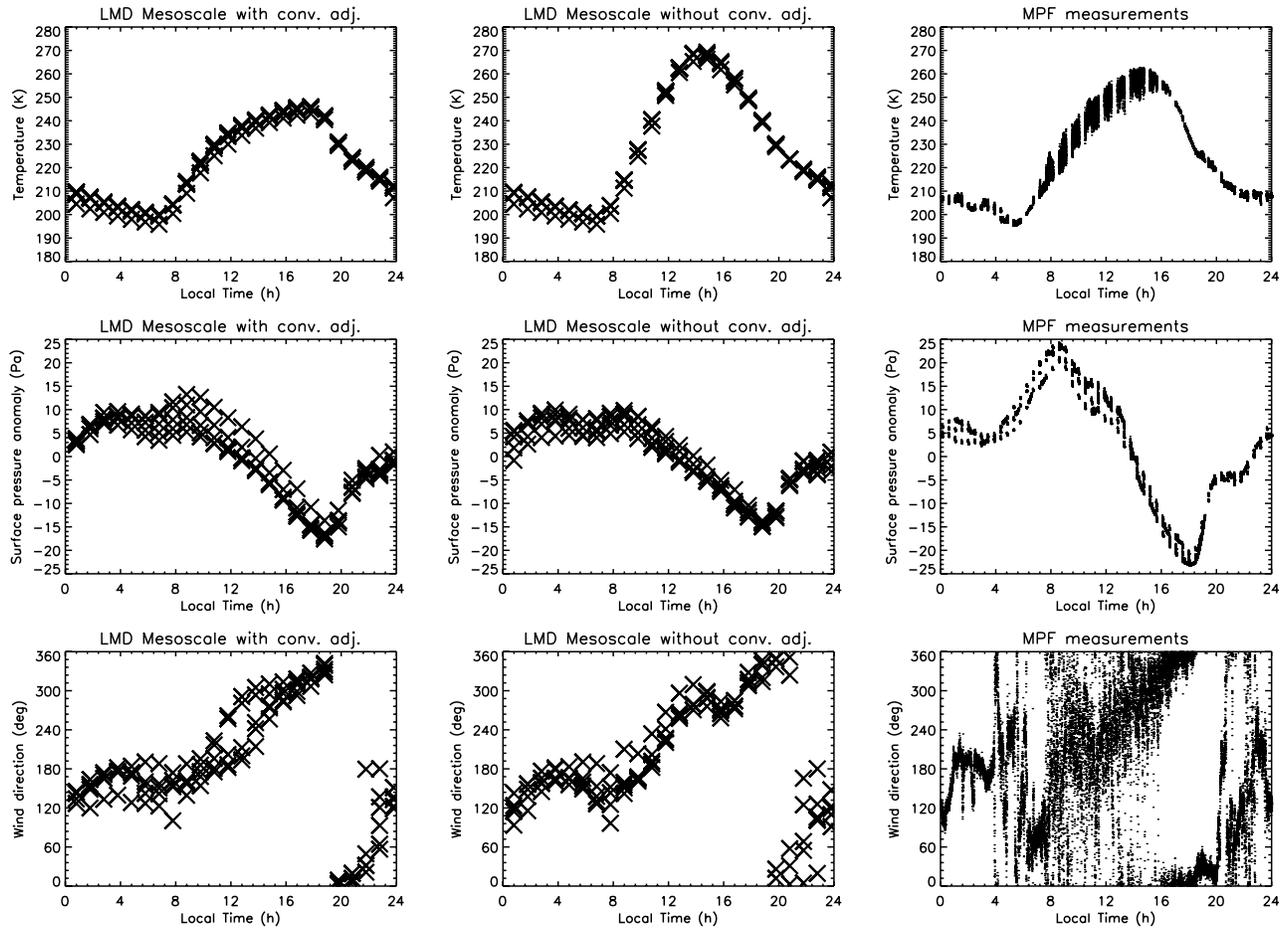
Figure 4. Same as Figure 3 at the Mars Pathfinder site. Lander coordinates are 33.10°W, 19.25°N; nearest grid point coordinates are 33.25°W, 19.10°N. Altitude of the lander temperature sensor is 1.27 m. Wind velocities are replaced by wind direction, as the error bars on the Pathfinder wind measurements might be rather high (see text for further discussion). J. Murphy kindly provided the Pathfinder wind data.

indicate the topography in Figure 5, as the increase in vertical velocity is closely related to the slope inclination.

[66] The near-surface slope winds are part of a general adiabatic recirculation of the atmospheric mass around the topographical obstacles. Cross sections of the canyon circulation along a given latitude (not shown) indicate that the near-surface anabatic winds are associated with a compensating downwelling of lesser amplitude in the center of the canyon, a few kilometers above the surface (the situation is reversed for katabatic winds). As emphasized by *Rafkin and Michaels* [2003], this secondary downwelling circulation induces adiabatic warming which acts as a positive feedback on the near-surface anabatic winds. This phenomenon has also been identified in modeling studies of terrestrial valley winds [*Rampanelli et al.*, 2004].

[67] The amplitudes of the thermally driven Martian slope winds in the Valles Marineris region differ from one study to the other, by about a factor of 1.5. Around $L_s \sim 320°$ (chosen to assess the atmospheric hazards at the MER proposed landing sites), *Rafkin and Michaels* [2003] found maximal afternoon updrafts reaching ~ 40 m s^{-1}, whereas *Toigo and Richardson* [2003] diagnosed maximal upslope winds of 25 m s^{-1}. Using their hydrostatic mesoscale model in the northern fall season, *Tyler et al.* [2002] found typical Valles

Marineris maximal upslope winds of ~ 20 m s^{-1}. The maximal vertical wind speeds on the walls of the canyon in these studies range from 5 to 10 m s^{-1}. With idealized boundary conditions, and a similar dynamical core as our model, the PlanetWRF model [*Richardson et al.*, 2007] predicts 5 m s^{-1} vertical winds on the flanks of the Valles Marineris canyon.

[68] LMD Martian Mesoscale Model simulations were carried out around $L_s \sim 320°$ to enable the comparison with the studies by *Rafkin and Michaels* [2003] and *Toigo and Richardson* [2003]. The LMD Martian Mesoscale Model predicts upslope daytime winds reaching $\sim 25-30$ m s^{-1} and downslope nighttime winds reaching $\sim 35-40$ m s^{-1} (note that the amplitudes in Figure 5 are slightly lower, owing to the influence of friction very near the surface). The maximal vertical winds on the walls of the crater are ~ 7 m s^{-1}, both in nighttime and daytime conditions. Thus, the order of magnitude of the Valles Marineris slope winds predicted by the LMD Martian Mesoscale Model is consistent with previous estimates in the literature. The lower velocity of the afternoon anabatic winds compared to the nighttime katabatic winds matches the conclusions drawn from 2-D mesoscale simulations by *Savijärvi and Siili* [1993].
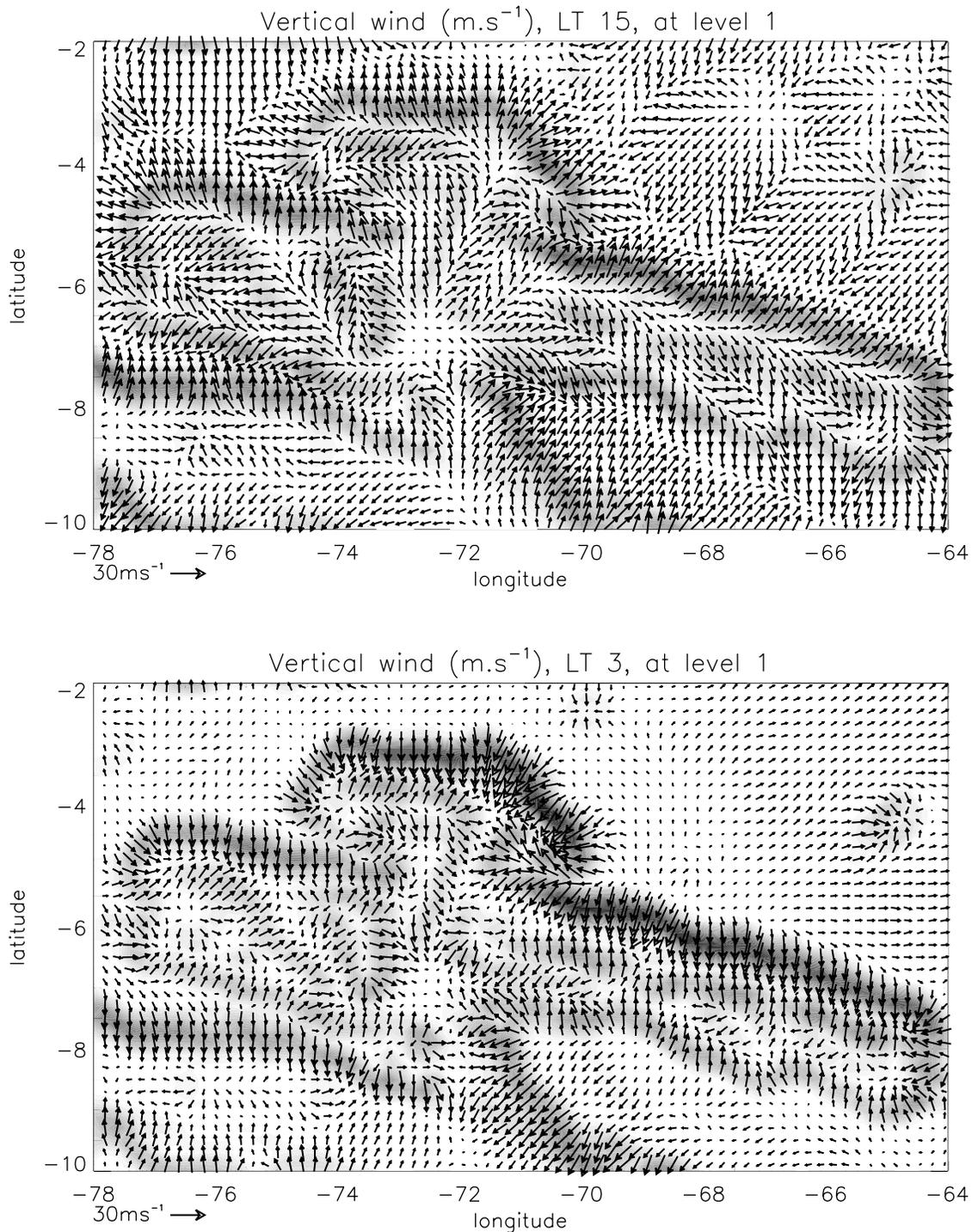
SPIGA AND FORGET: MARS MESOSCALE MODEL

Figure 5. Instantaneous near-surface wind field in the Valles Marineris canyon for (top) daytime and (bottom) nighttime conditions. Vertical wind magnitude is shaded; white represents magnitudes below $0.5 \, \mathrm{m \, s^{-1}}$; and dark grey corresponds to the maximal vertical velocity of $7 \, \mathrm{m \, s^{-1}}$. The displayed area is only part of the whole simulation domain, which has an extent of $[110°W-30°W] \times [20°S-4°N]$. Horizontal wind vectors are superimposed for every grid point. The wind field at the first model level is shown here, which corresponds to roughly 2.5 m (3.3 m) above the surface in nighttime (daytime) conditions. Note that velocities are expressed in the physical *xyz* space (i.e., the wind is decomposed into the three usual meteorological components (*u*, *v*, *w*)).
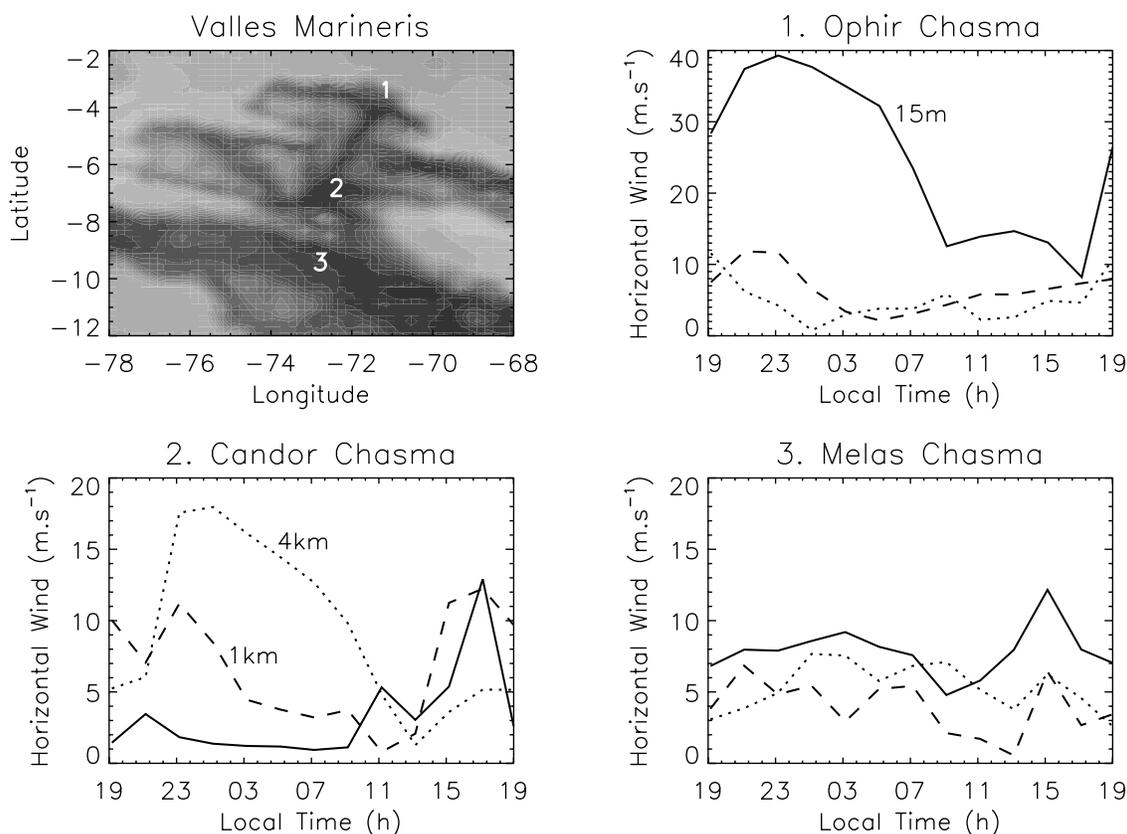
Figure 6. Daily cycle of near-surface horizontal wind magnitude in the Valles Marineris canyon. Data are shown every 2 h. Full, dashed, and dotted lines represent the horizontal wind 15 m, 1 km, and 4 km above the local surface, respectively. Three typical examples are given: (1) Ophir Chasma, near the walls of the canyon, where the largest near-surface nighttime wind velocities were diagnosed in Figure 5, (2) Candor Chasma, in the center of the topographical depression, and (3) Melas Chasma, in the middle of the plains within the canyon. The three chosen grid points are close in longitude; each indicated local time thus corresponds approximately to the same universal time. Note that the *y* scale in the two bottom plots is reduced compared to the top plot.

[69] To check the sensitivity to model resolution, we compared the predictions of the LMD Martian Mesoscale Model with horizontal resolutions of 18, 12, and 6 km. These simulations were carried out with the same vertical resolution, the same time step of 10 s and the same Valles Marineris topographical field at a lower resolution of 24 km (the number of grid points was chosen accordingly: 100×100 for $\Delta x = 18$ km, 150×150 for $\Delta x = 12$ km, 300×300 for $\Delta x = 6$ km). One of the motivations of this test was to investigate a possible underestimation of the slope winds with increasing resolution. This numerical bias is induced by enhanced numerical diffusion along terrain-following coordinates, and appears to be particularly critical on steep slopes [*Zängl*, 2002].

[70] Modifying the horizontal resolution led to wind speed differences less than ± 1.5 m s^{-1}. The simulated wind speeds are thus fairly independent of the chosen mesoscale horizontal resolution, and the aforementioned numerical bias does not appear as significant in our model. Actually, once identified by *Zängl* [2002], this problem was corrected in most mesoscale models, including the ARW-WRF dynamical core. We think, however, that the question was worth being addressed in Martian applications where intense circulations occur near dramatic topographical slopes.

[71] The uneven topography of Valles Marineris does not only drive powerful slope winds, but also acts as a "mechanical" obstacle for the atmospheric flow. Figure 6 illustrates this variety of wind regime. As was discussed previously, the flow in Ophir Chasma is mostly driven by the katabatic and anabatic winds near the surface. On the contrary, during the night, moderate winds near the surface are predicted in Candor Chasma, whereas wind amplification due to topographical channeling occurs at higher altitudes above the shallow boundary layer. This phenomenon could be due the alignment of the north-south central topographic channel in Candor Chasma, with the downslope wind direction further north on the Ophir Chasma rims (this interpretation is supported by a horizontal wind field section at the absolute altitude -1 km; figure not shown for the sake of brevity). Though less intense, wind acceleration within the narrow topographical corridors of Candor Chasma also occurs during the day, and accounts for the comparable values at 15 m and 1 km above the ground.

[72] Winds in Melas Chasma, far from the canyon rims, are of moderate amplitude throughout the whole day, in accordance with the wind behavior that could be encountered in the surrounding plains outside the canyon. This tends, for instance, to confirm that mesoscale atmospheric conditions are

favorable to haze formation into the canyon in the morning, as observed by MEx [*Inada et al.*, 2008].

[73] Finally, the vertical winds are very low (<1 m s^{-1} during the whole day) both in Candor Chasma and Melas Chasma, in agreement with previous diagnostics for MER landing site selection which did not rule out the spacecraft landing in the Valles Marineris canyon, on the condition that the canyon walls were located far enough away.

3.4. Large-Eddy Simulations in Gusev Crater

[74] Three-dimensional large-eddy simulations (hereinafter referred to as LES) aim to simulate the boundary layer processes by refining the horizontal resolution to ≲100 m, which enables one to resolve the part of the turbulence spectrum ("large eddies") responsible for most of the energy transport within the PBL. Significant insights on the PBL structure were obtained from idealized 1-D [*Haberle et al.*, 1993; *Savijärvi et al.*, 2004] and 2-D [*Odaka et al.*, 1998] models. Compared to these preliminary models, and besides the obvious realistic improvement gained by the three-dimensional computations, LES allow fewer initial assumptions and parameterizations to be made.

[75] LES can be carried out by specific idealized models [*Sorbjan*, 2006], or by appropriately lowering the horizontal resolution of fully compressible nonhydrostatic mesoscale models [*Toigo et al.*, 2003; *Michaels and Rafkin*, 2004]. The main advantage of the second approach (chosen in the present study) is that the thermal forcing of the PBL is provided by realistic computations of the radiative processes in the atmosphere. In addition, the use of the ARW-WRF dynamical core at microscale resolution has proved to be successful in representing PBL processes on Earth [*Antonelli and Rotunno*, 2007]. Despite theoretical and modeling efforts, knowledge of the PBL dynamics on Earth and on Mars remains incomplete, and is still in need of further observational evidence.

[76] LES were carried out with the LMD Martian Mesoscale model from 0830 to 1800 local time (LT) with the appropriate horizontal and vertical resolution (see Table 1), which must be of the same order of magnitude to properly simulate the 3-D convective motions. The horizontal mixing and the Knievel diffusion were removed for these LES applications; thus, the only dissipation is performed by the "natural" odd-order ARW-WRF advection technique. Subgrid-scale vertical mixing is performed by the aforementioned Mellor and Yamada scheme. Periodic boundary conditions were used to simulate the situation of an infinite flat plain. The simulation season and surface properties were chosen accordingly with the observation conditions for the Mini-TES instrument on board MER/Spirit [*Smith et al.*, 2006]. Random (noise) perturbations of 0.1 K amplitude were added to the initial temperature field to break the symmetry of this initial field and to help trigger convective motions [*Michaels and Rafkin*, 2004].

[77] After a few hundreds of seconds of spin-up time, the results of the LES can be analyzed. Figure 7 shows the evolution of the PBL thermal structure during the day. A super-adiabatic near-surface layer is present in the morning in the first 100 m, and a near-neutral mixing layer develops above this shallow inversion layer. The near-surface temperature profiles predicted by the LMD Martian Mesoscale Model are consistent with the equivalent profiles retrieved by Mini-TES (M. J. Wolff, personal communication and data delivery, 2008).

However, in the morning, the LES profiles are warmer by ~5 K than the Mini-TES profiles. As discussed in section 3.2, this may be related to the high sensitivity of the surface and near-surface temperatures to the assumptions made on surface properties and the amount of dust in the atmosphere. Moreover, the initial profile in the LES, derived from GCM simulations, is only an average over a large region. Nevertheless, the agreement between the temperature profiles predicted by the LES and the Mini-TES measurements is much better in the afternoon, as the warm "offset" in the LES temperature disappears at the end of the morning. Thus the slight temperature mismatch in the morning should not affect the main characteristics of the PBL dynamics discussed below (we consider that initializing the LES with a Mini-TES profile would have somewhat altered the comparison between the model and the data).

[78] The potential temperature profiles enable an estimation of the depth of the mixing layer, which attains a maximum altitude of roughly 5.5 km during the afternoon, in accordance with diagnostics in the aforementioned literature. The three-part vertical structure of the PBL can be clearly inferred from those profiles: unstable layer near the ground, neutral (mixing) layer in the core of the convective boundary layer, and stable (free atmosphere) layer at the top of the PBL. Interestingly, the temperature variations around 1330 LT are not unlike the variations measured by the in situ Mini-TES instrument [see *Smith et al.*, 2006, Figure 15]. This is an encouraging point, though we cannot go much further into the quantitative comparison between the model and the Mini-TES observations. Rigorous comparisons between LES and Mini-TES measurements would at least necessitate a conversion of the model temperatures into radiances, and an assessment of the effects associated with the nonverticality of the Mini-TES observations. We consider such work to be beyond the scope of the present paper.

[79] LES statistics are summarized in Figure 8. The growth of the convective boundary layer can be inferred from the turbulent kinetic energy (TKE) evolution, with the maximum altitude being reached by 1500 LT. Note that only the contribution of the LES resolved motions is considered in the TKE computations described in Figure 8. The quantity we call TKE for the sake of brevity should in reality be named the "large-eddy TKE" or "convective TKE," since the subgrid-scale Mellor-Yamada TKE is not included in the calculations. Around 1700 LT, as could be expected from the temperature profiles in Figure 7, the convective activity in the Martian PBL rapidly declines when the near-surface super-adiabatic layer begins to be replaced by the evening/nighttime stable layer. The evolution and the maximal amplitude of the TKE and the vertical TKE compare well with estimates by previous studies [*Michaels and Rafkin*, 2004; *Tyler et al.*, 2006]. The LES by the LMD Martian Mesoscale Model confirm that the contribution of the vertical term $\langle z'^2 \rangle$ to the total TKE is usually over 50%. As stated in those studies, such TKE amplitudes show that the Martian convection is two to three times more vigorous than on Earth, and is anisotropic with a clear tendency for strong vertical eddies, whereas the terrestrial partitioning tends to be isotropic.

[80] The vertical eddy heat flux variations are also of the same order of magnitude (maximum upward heat flux of 2.6 K m s^{-1}, maximum downward heat flux of -1.1 K m s^{-1}) as previous studies' estimates, which confirms that the
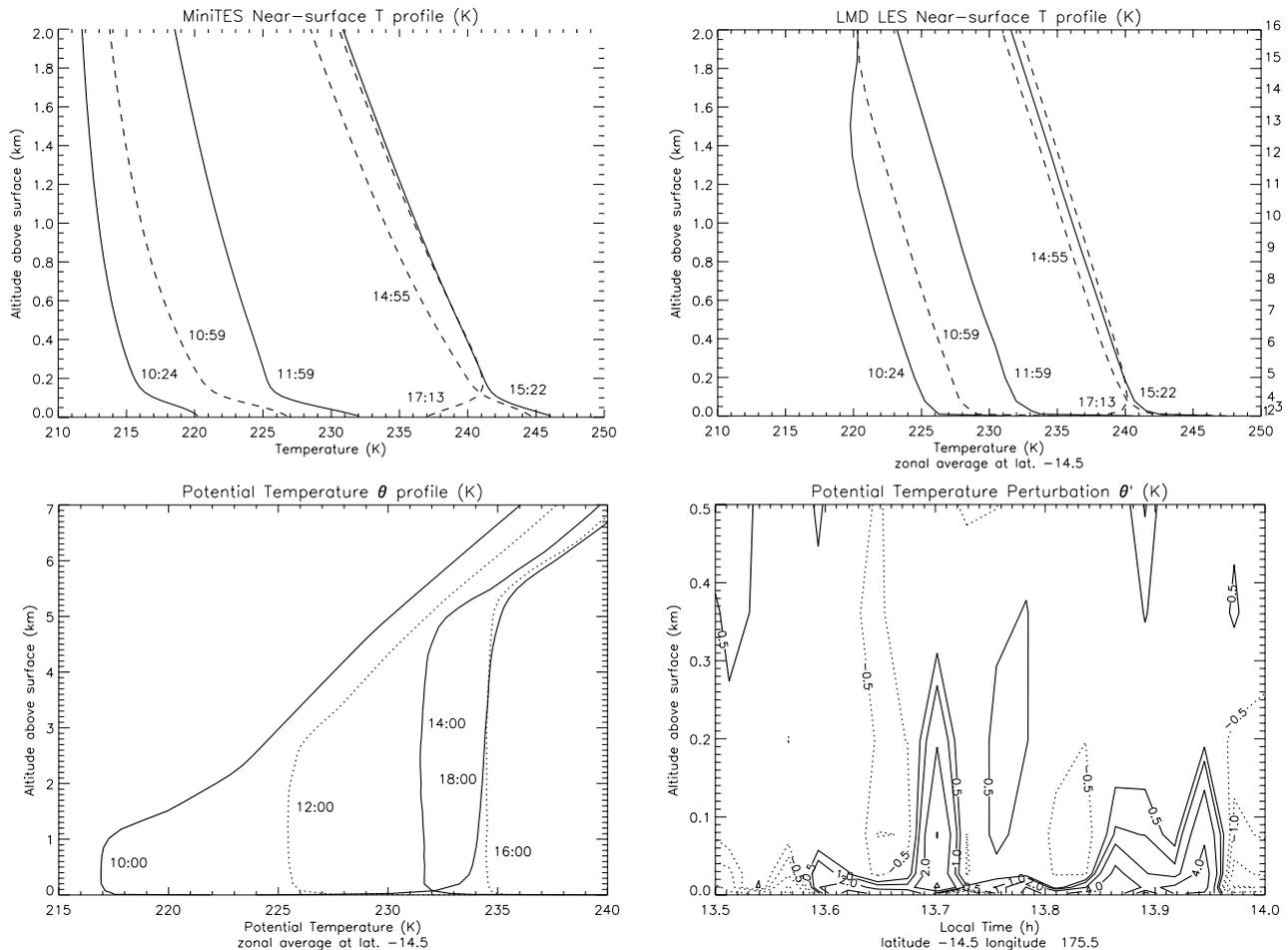
Figure 7. Temperature profiles in the Martian Planetary Boundary Layer (PBL). (top left) Mini-TES vertical profiles of temperature in the first 2 km above the ground, with additional refinements compared to the initial *Smith et al.* [2006] retrievals (data kindly provided by M. J. Wolff, and refinements described by Z. Sorbjan et al. (Temperature and turbulent heat flux profiles on Mars based on Mini-TES observations, submitted to Icarus, 2008). Dashed lines correspond to $L_s = 2°$, and full lines correspond to $L_s = 3°$; local times are given for each profile. (top right) Corresponding profiles as simulated by the LMD Mesoscale Model run in LES mode. The displayed profiles are zonally averaged to show the mean structure. The model vertical levels are indicated on the right side of the plot for reference. (bottom left) Vertical profile of modeled potential temperature in the first 8 km above the ground. Starting from 1000 local time, profiles are given each 2 h to the end of the afternoon. Zonal averaging is similar to the top right plot. (bottom right) Sample of the modeled potential temperature perturbations between 1330 and 1400 LT in the first 500 m (∼7 model levels) above the ground. Note that the corresponding plot for temperature is almost exactly similar. Maximal temperature variations are ±4 K, very close to the surface. Figure 7 can be compared to similar Mini-TES diagnostics in Figure 15 of the *Smith et al.* [2006] paper.

Martian boundary layer is less efficient than the terrestrial boundary layer in mixing heat. The transition between upward heat flux and downward heat flux occurs at roughly 80% of the mixing layer height, in agreement with the dimensionless LES results by *Sorbjan* [2006]. As explained in more detail by *Michaels and Rafkin* [2004], the vertical variations of the vertical eddy heat flux indicate whether PBL convection induces a warming (decreasing flux with z) or a cooling (increasing flux with z) of the atmosphere. It could be deduced from Figure 8 (top right) that the Martian PBL convection cools the atmosphere very near the surface, but warms the atmosphere just above, in the lowest part of the mixing layer. This is consistent with the fact that the near-

surface Martian atmosphere receives a significant fraction of its total energy by absorption of infrared radiation incoming from the surface [*Haberle et al.*, 1993; *Savijärvi et al.*, 2004], rather than overwhelmingly from the surface itself by conduction, as is the case on Earth. As PBL turbulent motions tend to mix heat to counteract the heating gradients, the Martian near-surface environment is thus cooled by convection, unlike its terrestrial counterpart.

[81] Figure 9 shows that the horizontal organization into polygonal cells is predicted by the model, with narrow updrafts and broad downdrafts, in conformity with the published literature. The cell size tends to increase during the end of the morning and beginning of the afternoon, following the
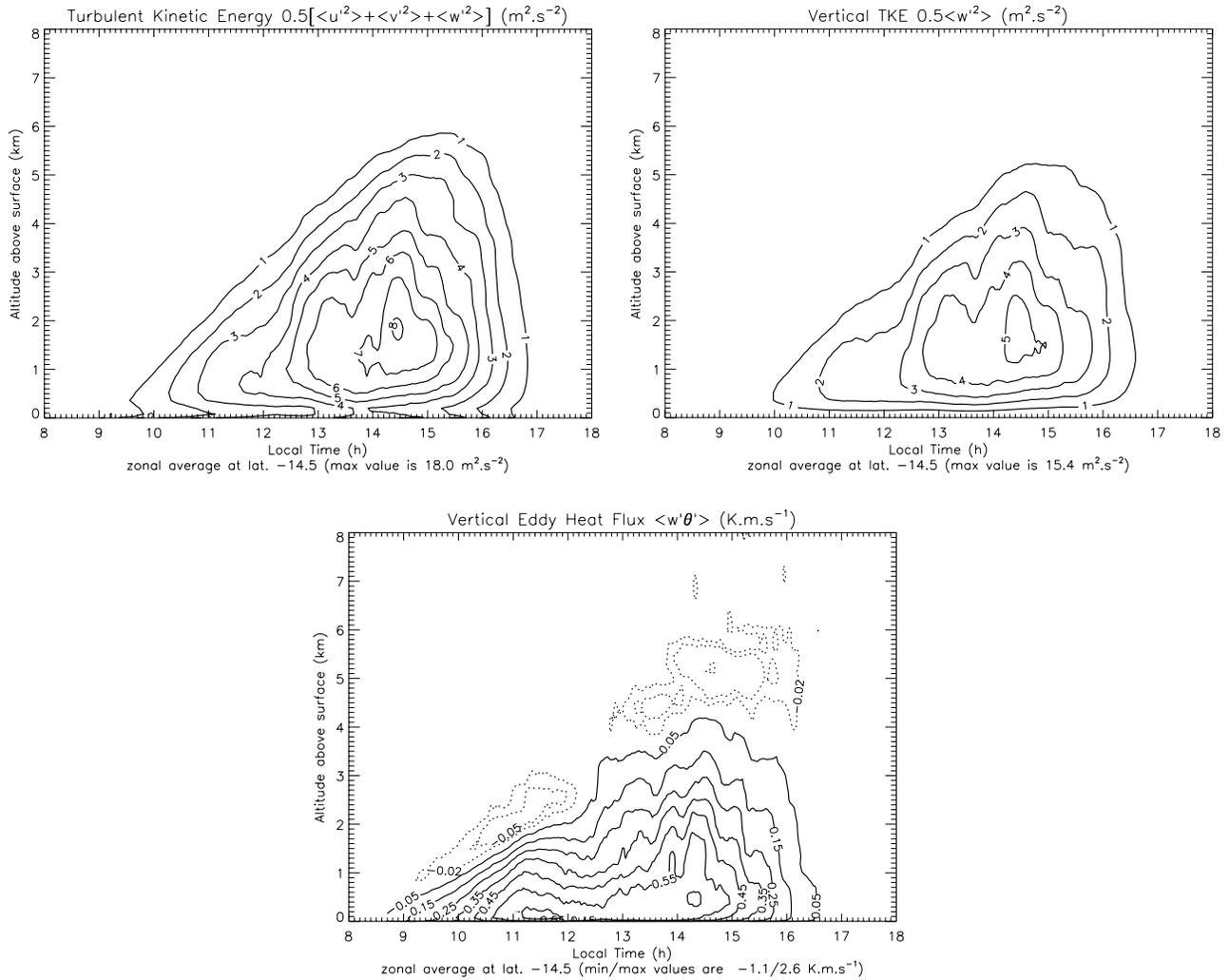
Figure 8. PBL statistics for the Gusev Crater simulation. Perturbations X' of a given field X are calculated by subtracting from the total field an average field $\langle X \rangle$ obtained by temporal smoothing with a window of 1 Martian hour. The "1 hour" smoothing window, usually employed in terrestrial studies, enables a clear filtering of the turbulent component; windows of half a Martian hour and of 2 Martian hours were comparatively less efficient. Once the perturbation fields are obtained, the same filtering window is employed in the averaging operations leading to the final value of (top left) the turbulent kinetic energy, (top right) the vertical turbulent kinetic energy, and (bottom) the vertical eddy heat flux. Zonal average over the indicated latitude is performed to yield the displayed diagnostics.

increase in PBL depth. The vertical velocity ratio between the updrafts and the downdrafts is approximately 2. The stably stratified free atmosphere above the convective boundary layer is perturbed by the updrafts, which gives rise to internal gravity waves, by a mechanism similar to lee wave generation [*Stull*, 1976]. Oscillations in the potential temperature field can indeed be observed on a longitude-altitude cross section. The horizontal wavelength of these waves is ~5–10 km. Owing to the propagation of these gravity waves, the upper part of the boundary layer is still active after the early evening rapid decline of the well-mixed layer below.

[82] At the intersection of the polygons formed by the updrafts, vortices appear above the horizontal limit resolution, in the beginning of the afternoon, until the collapse of the convective boundary layer. The width of these vortex structures is ~300–500 m, and the corresponding depres-

sion is of the order of 1 Pa. An enhanced view is shown in Figure 9, centered on the maximal depression structure of ~1.5 Pa, which is larger and deeper than the regular structures owing to the conjunction of two vortices. On the walls of the vortex, horizontal winds reach 10 m s^{-1}, well above the "regular" turbulent horizontal gustiness of ~4 m s^{-1} in the domain, and upward vertical winds reach 8 m s^{-1}. Negligible vertical and horizontal velocities are observed within the vortex core. The lifetime of this convective vortex is approximately half an hour, though other events were more short lived (1000–1500 s).

[83] Thus, the observed vortex shares all the characteristics of a cyclostrophically balanced vortex as theoretically described by *Rennó et al* [1998], modeled by *Toigo et al.* [2003], and identified by *Ferri et al.* [2003] in the Pathfinder data (albeit the depression was deeper in the case of the Pathfinder
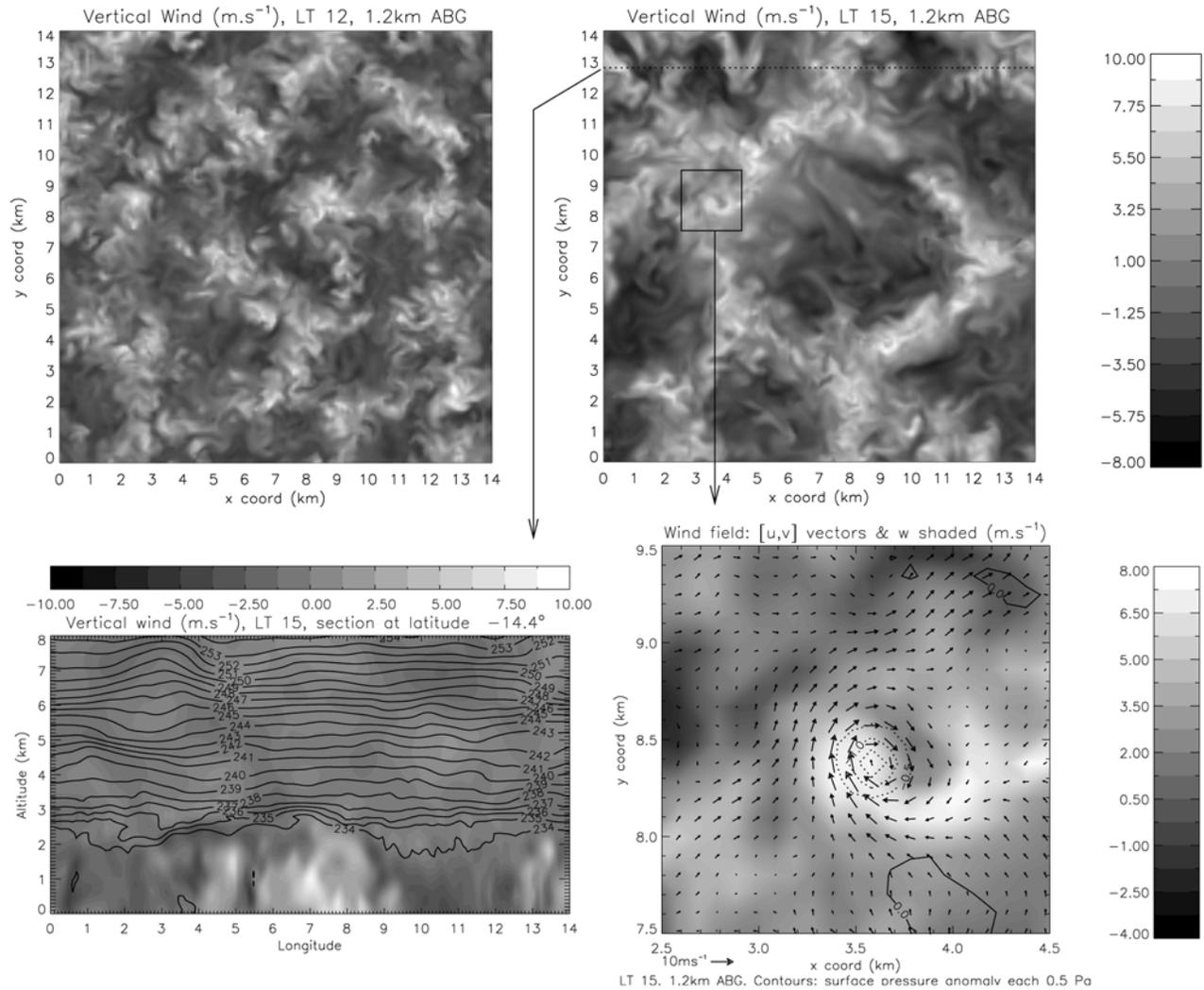
Figure 9. Instantaneous view of the simulated atmospheric circulation at microscales in Gusev Crater. (top) Vertical velocity horizontal section 1.2 km above the surface, showing the entire simulation domain. Updrafts are represented in white; downdrafts are in black. Each kilometer comprises 10 grid points, enabling a fine representation of the "large-eddy" part of the turbulence spectra, as can be observed in the images. Instantaneous fields at (left) 1200 LT and (right) 1500 LT are provided to give clues on the evolution of the polygonal structure of the convective cells. (bottom) Insights into the shaded vertical velocity field of the top right image. Note that the black and white scales are different. (bottom left) Longitude-altitude cross section of vertical velocity with potential temperature contours superimposed (1 K spacing). Note that the model top is ∼11 km. (bottom right) Enhanced view of a particular vortical structure. Horizontal wind vectors are superimposed, as well as contours corresponding to the surface pressure perturbation (0.5 Pa spacing), obtained by subtracting from the raw surface pressure field an average surface pressure value over the whole domain. Maximal depression in the vortex core is ∼1.5 Pa.

vortex). If dust can be lifted and transported into these vortical structures, these might give rise to well-known dust devil features. The fact that the Spirit MER recorded numerous images of passing dust devils within Gusev Crater is another suggestive clue that one may consider the modeled vortices to be "dust devils without dust."

[84] The horizontal resolution of 100 m only enables one to resolve the larger vortices. Furthermore, Gusev crater conditions may be more sophisticated than the rather idealized simulation proposed here: (1) The sensitivity of the number and intensity of the dust devils with thermal inertia, season, and location has to be studied to assess if Gusev Crater is a preferential location for dust devil formation. (2) The "no-wind" case presented here does not take into account the influence of the crater's background mesoscale wind, which could significantly affect the dust devil formation and transport. (3) The topography may locally trigger or enhance convection.

[85] Even if further work involving models and observations is needed to yield a more comprehensive view of the Martian PBL, the results of the LMD Martian Mesoscale Model are promising, and in very good agreement with

previously performed independent Martian LES. The preliminary comparison with the Mini-TES profiles is also very encouraging.

3.5. Tharsis Clouds

[86] In the LMD Martian Mesoscale Model, the water cycle is simulated by coupling the transport of the atmospheric water by the dynamical core (presently two tracers are used, one for ice and one for vapor) with the physical parameterizations described by *Montmessin et al.* [2004] for turbulent mixing, surface ice sublimation, sedimentation

Water ice cloud opacity at 0.4 μm, LT 16

Ls 120 − White: < 0.2 − Black: > 0.8

Water ice cloud opacity at 0.4 μm, LT 4

Ls 120 − White: < 0.2 − Black: > 0.8

processes, atmospheric water ice condensation and particle growth.

[87] The initialization and boundary prescription of humidity fields in Earth mesoscale models is particularly difficult. Usually, specific corrections and caveats are needed to avoid spurious latent heat release, triggering of convective systems at the wrong locations, or producing unrealistic convective instabilities [e.g., *Diongue et al.*, 2002]. Thus, for the sake of simplicity, only the water vapor mixing ratio (and not the mixing ratio of the various cloud species such as droplets, ice, graupels…) is extracted from the GCM simulations and transported through the boundary conditions of the mesoscale parent domain. On the contrary, the Martian water cycle and the associated meteorological dynamics are not strongly influenced by the latent heat release (respectively, consumption) when clouds form (respectively, dissipate), as the low quantities of water involved yield negligible latent heat transfer. A priori, the water ice mixing ratio can thus be prescribed at the boundaries without any particular caution. A posteriori, this approach did not seem to lead to particularly serious issues, as a rather continuous behavior of the two involved water tracers is observed at the boundaries during the simulations.

[88] For decades, water ice clouds have been observed between midspring and midsummer in the vicinity of the Tharsis and Olympus Mons volcanoes [*Peale*, 1973; *Benson et al.*, 2003]. Numerical simulations by *Michaels et al.* [2006] confirmed the rich mesoscale dynamics involved in the formation of these clouds. Reproducing the cloud structure near the volcanoes is thus an interesting indirect validation for the LMD Martian Mesoscale Model.

[89] Typical daytime and nighttime cloud cover obtained by the LMD Martian Mesoscale Model in the Tharsis region at $L_s \sim 120°$ ("aphelion cloud belt" season) are given in Figure 10. The model reproduces the distinctive cloud concentration on the western flanks of each volcano. The afternoon water ice cloud opacity map of Figure 10 is reasonably similar to the numerous images acquired by the MOC camera [*Wang and Ingersoll*, 2002] and the MARCI wide-angle device [*Malin et al.*, 2008]. Both in the observations and in the model, the clouds in the vicinity of Olympus Mons are optically thicker than the clouds formed on the other three Tharsis volcanoes. A noticeable difference, however, is that the observed Tharsis clouds are in general slightly optically
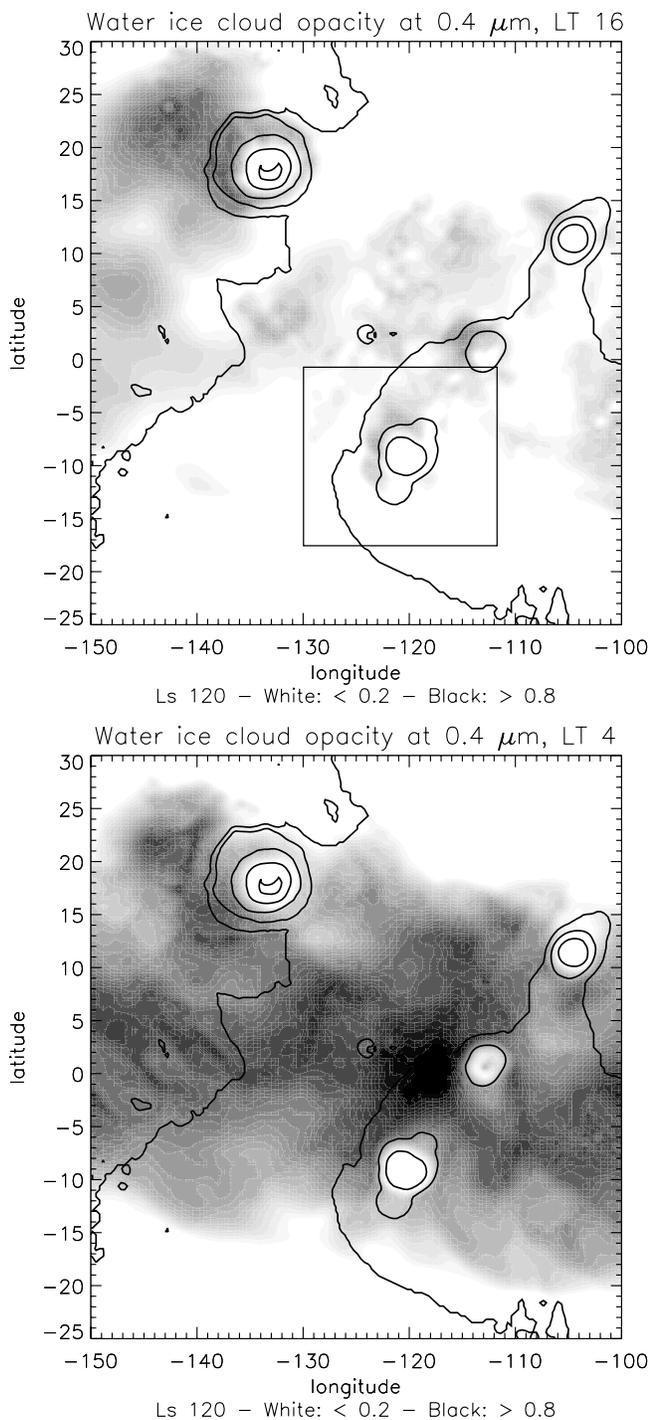
Figure 10. Water ice cloud visible opacity in the Tharsis region at $Ls = 120°$ for (top) daytime and (bottom) nighttime conditions. The Arsia nest is delimited in the top plot (see Figure 12). Visually opaque clouds are in black (maximal opacity is 0.9); very thin clouds (or no clouds at all) are in white. The cloud opacity is computed at 0.4 μm using the formula $\tau = \frac{3m}{4\rho\langle r \rangle} Q_e$, where m is the water ice total column (kg m^{-2}), $\langle r \rangle$ is the average radius in the column (computed as the mean of the radius in each layer weighted by the total amount of ice in the considered layer), ρ is the density of water ice 917 kg m^{-3}, and Q_e is the extinction efficiency at 0.4 μm. The latter parameter is calculated (assuming ice spheres) by $Q_e = \frac{C_e}{\pi r_0^2}$, with $C_e = 20.613$ μm^2 being the extinction cross section at wavelength 0.4 micron for ice particle radius of $r_0 = 2$ μm (M. J. Wolff, personal communication, 2008), which yields $Q_e \sim 1.64$.
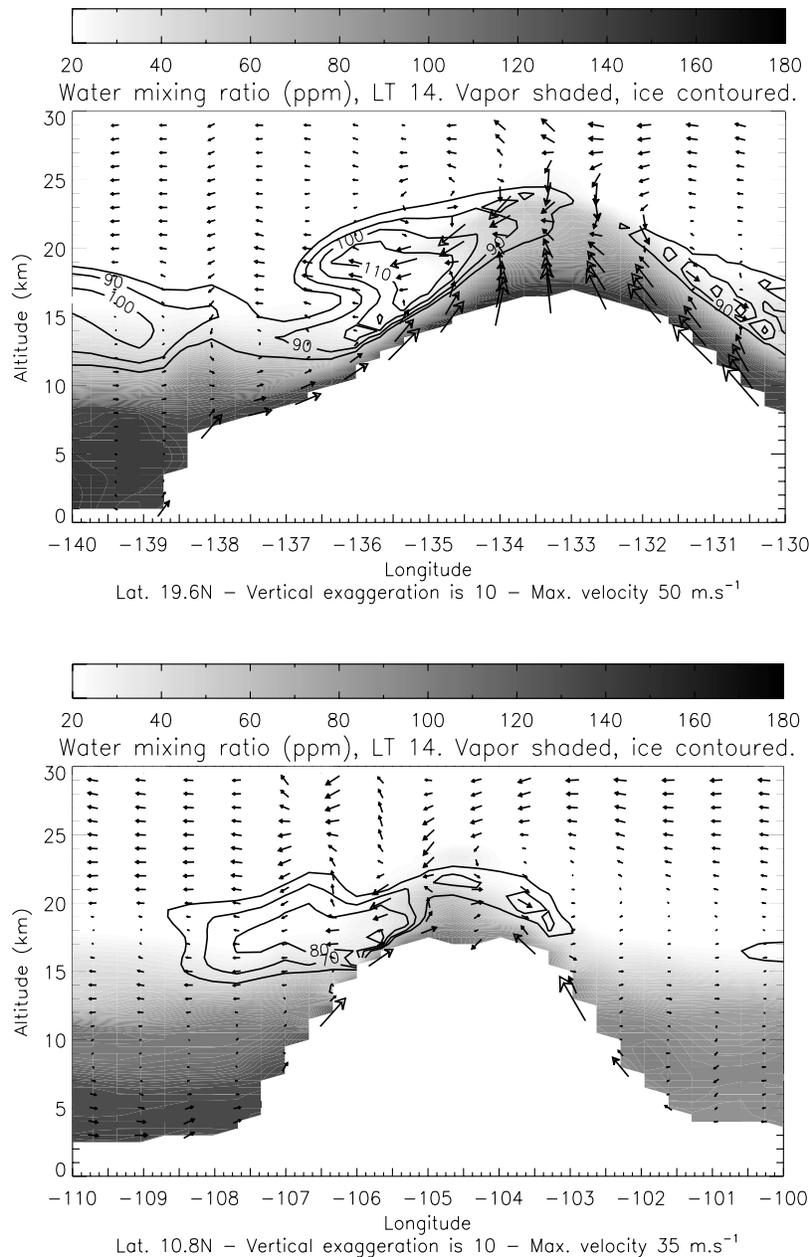
Figure 11. Longitude-altitude cross section of water mass mixing ratio at $L_s = 120°$ for (top) Olympus Mons and (bottom) Ascraeus Mons. Water vapor is shaded; water ice is contoured. Fields were interpolated from model levels to altitude levels by hydrostatic integration. Wind vectors composed of the vertical and zonal velocity components are superimposed. Note that the vertical scale is exaggerated by a factor of 10. Though the annotations on the x axis are in degrees longitude, the plot was generated with a kilometer-scaled x axis to account for the real orientation of the wind. The maximal wind velocity is consistent with previous studies' estimates [*Nayvelt et al.*, 1997; *Rafkin et al.*, 2002].

thicker and have a larger western extent than the modeled clouds presented here. Note that an alternative LMD Martian Mesoscale Model simulation performed at $L_s = 90°$ yields similar structure, orientation and opacity of the clouds, consistently with the particular repeatability of these structures observed in MOC and MARCI images during northern spring and summer.

[90] The main dynamical mechanism involved in the formation of the clouds is the strong water vapor advection by the afternoon upslope winds [*Leovy et al.*, 1973; *Michaels et al.*, 2006; *Maltagliati et al.*, 2008] above the hygropause, i.e., the level above which the water vapor mixing ratio rapidly declines (in our example, the altitude of the hygropause is $\sim 10-15$ km). This topographically driven cloud formation is particularly efficient as the Tharsis region is characterized by low thermal inertia, which ensures a rapid onset of the afternoon upslope winds shortly after the insolation maximum. The water vapor upslope advection can be clearly identified in the longitude-altitude cross sections of Olympus Mons and Ascraeus Mons in Figure 11.

In the case of Olympus Mons, water mass mixing ratios are in reasonable agreement with the predictions by *Michaels et al.* [2006] (their Figure 2), though our predicted water ice mixing ratios are roughly multiplied by a factor of 2 compared to the *Michaels et al.* [2002] values; the diagnostic is similar for the $L_s = 90°$ simulation. Additionally, mountain wave activity can be observed by the alternating patterns of positive/negative vertical velocities (figure not shown), which contributes to the shape of the observed clouds, as already noticed by the aforementioned authors.

[91] The altitudes of the clouds predicted by the LMD Martian Mesoscale Model are compatible with the MOC observations by *Benson et al.* [2003], with mean afternoon cloud altitudes of ∼20 km on Olympus Mons and ∼17 km on Ascraeus Mons. Though this quantitative agreement is an encouraging point, microphysical refinements are still needed to fully understand the cloud formation. For example, the fact that particle radii reach sizes of 8 and even 10 μm in the afternoon clouds over the volcanoes necessitates further investigation for confirmation. Recent measurements carried out by MEx/OMEGA [*Madeleine et al.*, 2008] or MRO/CRISM [*Wolff et al.*, 2008] will be very helpful in the future to assess the plausibility of the mesoscale models' cloud predictions. Furthermore, *Wilson et al.* [2007] demonstrated the strong radiative influence of water ice clouds on the temperature field and the atmospheric circulation. Including this critical effect in the LMD Martian Mesoscale Model would improve the knowledge of the clouds formation and the associated feedbacks.

[92] Recently, the extensive nighttime cloud cover was also studied in detail by *Wilson et al.* [2007, Figure 3] using nighttime TES and MOLA measurements. This cloud cover is reproduced by the LMD Martian Mesoscale Model, with a maximum in opacity in the plains between the Tharsis trio and Olympus Mons. Nighttime clouds are significantly thicker than their daytime counterparts. No clouds are predicted at the summit of the volcanoes; the altitude of the night cloud deck is ∼10 km altitude, just above the hygropause.

[93] The improved resolution (∼5 km) of the one-way nest centered on Arsia Mons enables a refined analysis of the cloud morphology. As can be seen in Figure 12 (top), water ice opacity in the vicinity of Arsia matches the opacity field obtained in the coarse-resolution parent domain (see Figure 10), though finer opacity variations are resolved by the model. *Wang and Ingersoll* [2002] showed for instance that Arsia is a preferential location for "aster" cloud formation during midsummer to late summer, consisting of radial structures at low altitudes and thicker and brighter cloud masses above the volcano. It can be seen in Figure 12 (bottom left) that the "aster" structure is not reproduced by the model. However, some radial organization of the clouds around the volcano is predicted in the simulations, as well as significant local variations of water ice mass mixing ratio. The small-scale variations of water ice content, associated with a more organized radial structure than what is predicted by the model, may give rise to an "aster" cloud feature identified in the observations (though the MOC images did not always show a perfect radial organization). At higher altitudes, above the Arsia Mons caldera, as shown in Figure 12 (bottom right), high quantities of atmospheric water ice are found, which might explain the central bright cloud described by *Wang and Ingersoll* [2002] (this central feature, however, hardly

appears on the opacity map, which may be due to smaller particle radii).

[94] The main mechanism accounting for the radial morphology of the Arsia clouds is still the atmospheric transport of water vapor along the volcano flanks by the afternoon upslope winds. However, further investigations show that the cloud structure is very sensitive to local-scale variations of vertical velocity (figures not shown), should they be convective motions in the first kilometers above the local surface, or internal gravity waves triggered by the interaction between the mean flow and the volcano. The shape of the clouds is modulated by the waves, which locally warm or cool the atmosphere and modify the local advection, by a mechanism similar to lee cloud formation.

3.6. Olympus Mons: The Nighttime "Warm Ring"

[95] The purpose of this section is to report an interesting mesoscale effect in the vicinity of the Olympus Mons volcano. The LMD Martian Mesoscale Model predicts a significant surface temperature enhancement, which can reach +20 K, during the night at the feet of Olympus Mons. This "warm ring" signature can be clearly seen in Figure 13 (left), showing the results of a northern fall simulation. The signature was, however, identified at various other seasons. The width of the ring is several grid points, which corresponds to roughly 30 to 70 km in extent. It is worth noticing that alternative areas of slighter warming can be observed in Figure 13 (left) in the vicinity of significant topographical gradients in the simulation domain.

[96] This nighttime "warm ring" is observed both in simulations including the regular thermal inertia field around Olympus, and in simulations assuming constant thermal inertia (which is the case of the displayed example). The rationale for running a LMD Martian Mesoscale Model simulation with constant thermal inertia is that the identified surface temperature signature shows a shape similar to the nighttime thermal inertia enhancement at the feet of Olympus [*Putzig and Mellon*, 2007]. Comparable simulation results with the two kinds of thermal inertia assumptions strongly suggest that the "warm ring" effect is controlled by the dynamics rather than the surface properties. The question might even be how such an effect could influence the nighttime thermal inertia retrievals. The temperature enhancement predicted by the LMD Martian Mesoscale Model is not taken into account in the thermal models used to retrieve the thermal inertia, likely causing an overestimation of this parameter. This interpretation is supported by the higher thermal inertia values at the feet of the Tharsis volcanoes in the high-resolution thermal inertia maps by *Putzig and Mellon* [2007].

[97] The nighttime warm ring around Olympus Mons can be interpreted as a direct consequence of the nighttime katabatic winds (Figure 13, right). The temperature enhancement results from adiabatic compression of air masses induced by the strong downwelling along the slopes of the volcano. An examination of the potential temperature field near the surface (figure not shown), closely following the temperature variations, confirms that the observed phenomena result from an adiabatic effect.

[98] Figure 13 shows that the atmospheric temperature has an excess of nearly 30 K above Olympus's rims. The temperature excess is not confined near the surface, but extends
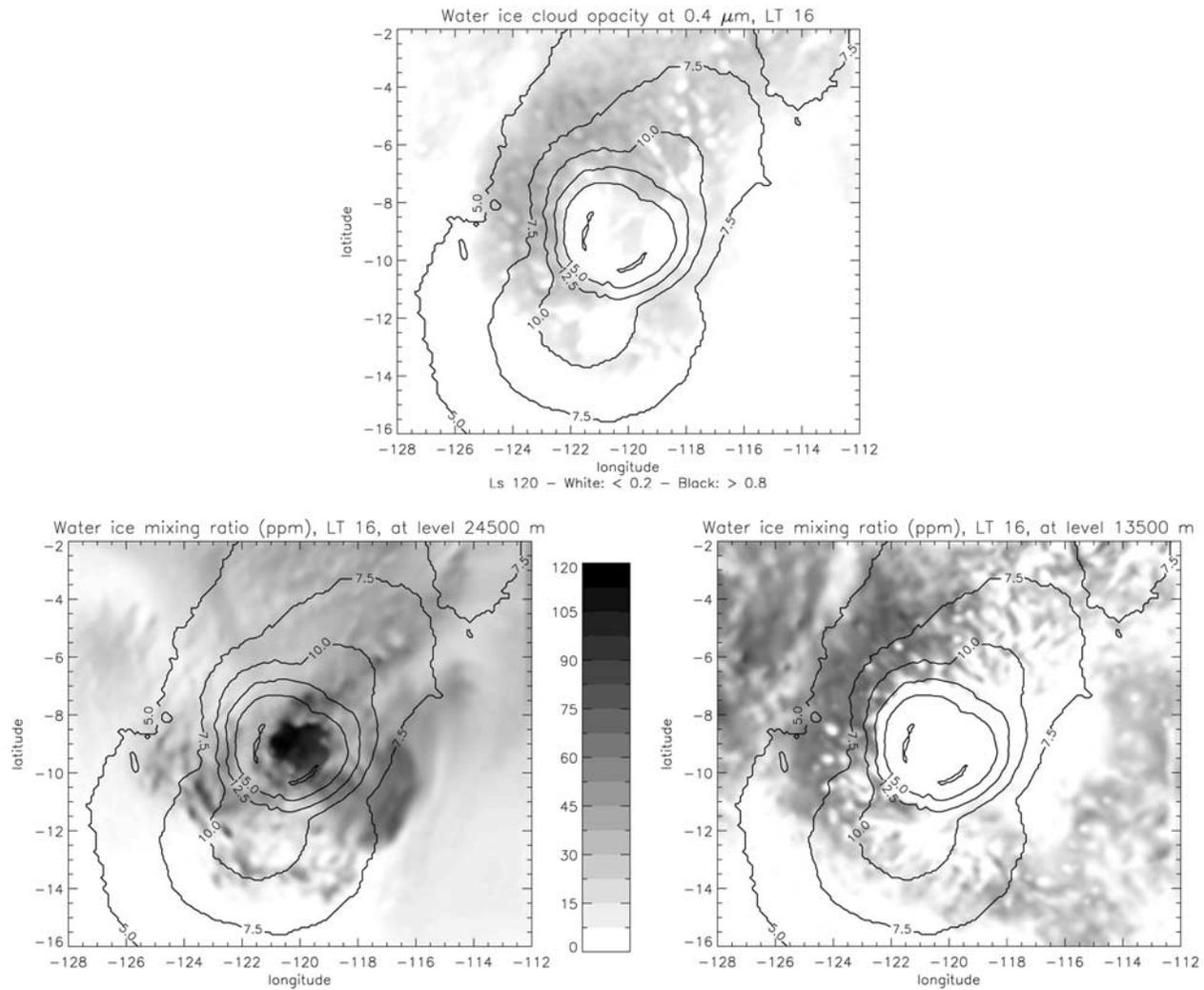
Figure 12. Clouds in the nested domain centered on Arsia Mons (5 km horizontal resolution). Topography contours at 5, 7.5, 10., 12.5, 15., and 17.5 km are superimposed. (top) Afternoon water ice cloud visible opacity. See caption of Figure 10 for details. (bottom right) Water ice cloud mass mixing ratio horizontal section at an altitude of 13.5 km above the MOLA reference. Missing values above 13.5 km appear as white on top of the volcano. (bottom left) Same as the bottom right plot, but at an altitude of 24.5 km (no missing values).

to 1–1.5 km above the local surface. The surface temperature increases as the warmer overlying atmosphere enhances the downward IR flux to the surface. The phenomenon arises quickly after sunset, owing to the low thermal inertia in the Olympus Mons region and the rapid onset of the katabatic flow, and persists all night long.

[99] A well-known terrestrial equivalent is the Santa Ana winds [see, e.g., *Raphael*, 2003]. Downslope circulation occurs from the elevated Mojave Desert (when the desert is particularly cold) to the Californian Pacific coastline, and adiabatically warms the air, which favors wildfires.

[100] The amplitude of the observed warming is obviously sensitive to the magnitude of the nighttime slope winds. Unfortunately, quantitative measurements of the winds close to the Martian topographical features are still lacking. However, as could be drawn from sections 3.3 and 3.5, predictions of slope winds by the LMD Martian Mesoscale Model are in

reasonable agreement with the results obtained by other independent models. The overall qualitative description of the "warm ring" phenomena can thus be considered as robust, albeit the quantitative estimate of the nighttime near-surface warming may be subject to revision, after further observational evidence. Such an effect emphasizes the need for 3-D mesoscale modeling, instead of simple energy-balance models, to determine surface temperature near the highest topographical obstacles.

4. Discussion

4.1. Summary

[101] The main conclusions of the study are the following:

[102] 1. The LMD Martian Mesoscale Model, based on the ARW-WRF dynamical core, is a versatile and promising tool to study the Martian atmospheric circulation at regional scales.
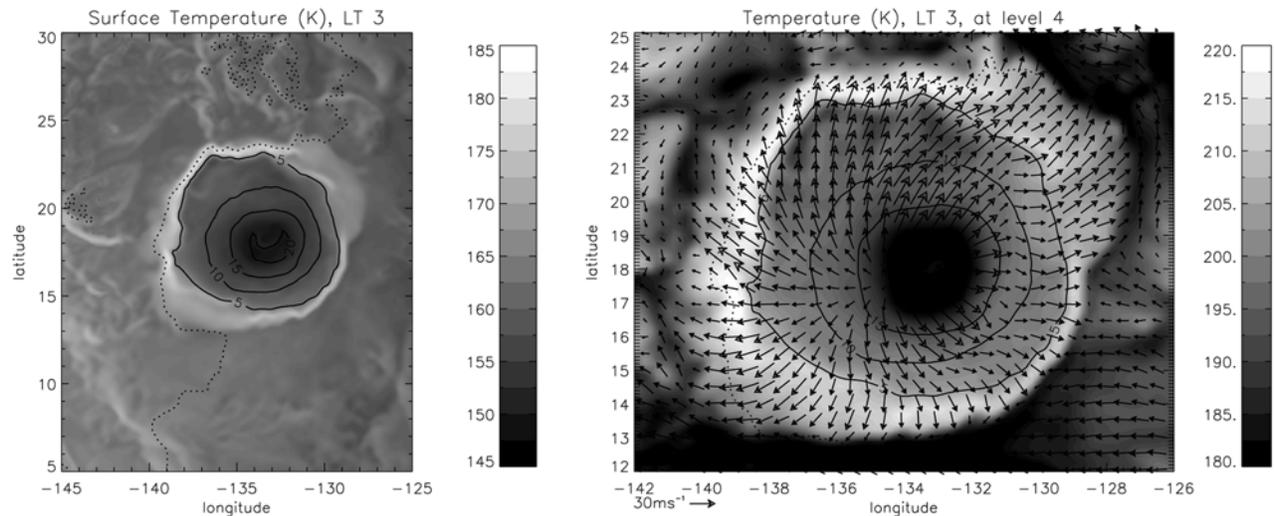
Figure 13. Nighttime adiabatic warming by downslope winds in the Olympus Mons area. Simulations are carried out with a constant thermal inertia of 85 J m^{-2} K^{-1} s$^{-0.5}$. (left) Surface temperature at local time 0300 LT. Warmer temperatures are white. Topographic contours are superimposed for reference (altitudes -2.5, 5, 10, 15, 20, and 25 km). (right) Atmospheric temperature at the 4th model level ($\sim$120 m above the surface). Horizontal wind vectors are superimposed every 3 grid points. Maximum horizontal wind velocity at this level is $\sim$40 m s^{-1} (above Olympus caldera). Warmer temperatures are white, and the topographic reference is the same as the left plot.

[103] 2. All the up-to-date physical packages developed for a decade for the LMD-MGCM applications are natively included in the model, which ensures (1) a comprehensive reproduction of the main atmospheric cycles: dust, CO_2, water, chemical species and (2) a high level of consistency between the forcing at the lateral boundaries of the mesoscale domain (derived from LMD-MGCM simulated fields) and the computations in the mesoscale domain themselves.

[104] 3. Correct initialization and definition of boundary conditions require the use, in the vertical interpolation process, of a terrain-following strategy near the surface, and pressure-based interpolations at higher altitudes.

[105] 4. The results of the mesoscale model in coarse-resolution mode, with free evolution in the longitudinal dimension, are consistent with the LMD-MGCM calculations for vertical thermal profiles, latitudinal atmospheric structure, and longitudinal tidal wave structure; differences result mainly from the limited model top.

[106] 5. Near-surface daily cycles of temperature, pressure, and horizontal winds are consistent with the VL1 and Pathfinder measurements on the condition that no convective adjustment is included in the model; note slightly warmer atmospheric temperatures near the surface in the model.

[107] 6. The mesoscale model demonstrates encouraging performance in microscale mode (large-eddy simulations) as (1) the main characteristics of the Martian PBL drawn by previous studies (mixing layer growth, turbulent heat fluxes, polygonal cell structure, convective vortices) are reproduced by the model and (2) the temperature profiles are to first order in satisfactory agreement with the Mini-TES recent measurements at the surface.

[108] 7. Qualitative and quantitative wind predictions in topographically uneven locations such as Valles Marineris, are in good agreement with the previously performed independent mesoscale simulations in the literature: (1) the fact

that intense upslope and downslope flow takes place along the Valles Marineris rims (reaching respective velocities of 30 m s^{-1} and 40 m s^{-1}, with a vertical component of 7 m s^{-1}) is confirmed by our model, and (2) the influence of the topographical channeling on the winds within the canyon is found to be significant.

[109] 8. The water ice clouds controlled by the Tharsis and Olympus Mons topographical obstacles are reasonably reproduced by the model, which predicts consistent altitudes of the afternoon clouds with respect to remote-sensing retrievals; high-resolution simulations in Arsia Mons give clues to the ''aster clouds'' structure, though the radial structure of these clouds is not clearly reproduced.

[110] 9. Adiabatic warming by the katabatic nighttime winds in the Olympus Mons region can cause surface temperature excess of +20 K at the feet of the giant volcano; this effect is thought to adversely affect the thermal inertia derivations in the Tharsis region.

4.2. Perspectives

[111] The possible applications of the LMD Martian Mesoscale Model are not restricted to the validation case studies shown in this paper. Numerous Martian mesoscale phenomena are in need of further analysis, or remain unknown. In addition to further investigation of the Martian boundary layer, of the wind regimes in topographically uneven areas, and of water ice clouds, work is already ongoing on the following topics at the time of this writing: (1) interpretation of the *Spiga et al.* [2007] surface pressure maps, (2) aeolian control on dune formation, (3) mesoscale dynamics at the onset of the 2001 global dust storm [*Montabone et al.*, 2008], (4) formation of the (convective?) high-altitude mesospheric CO_2 ice clouds observed by *Montmessin et al.* [2007], and (5) wake dynamics in the lee of Elysium Mons. The use of the LMD Martian Mesoscale Model is also being considered for

the following applications: (1) polar dynamics and polar night processes (CO_2 ice clouds), (2) local atmospheric processes in Martian paleoclimates (formations of glaciers, gullies), (3) comparative study of the diagnostics obtained with or without the hydrostatic assumption, and (4) evaluation of atmospheric hazards at the selected landing sites for future missions.

[112] Upgraded LMD-MGCM physical packages, taking advantage of the recent measurements by the instruments on board MEx and MRO, will be included in the LMD Martian Mesoscale Model as well. As the spatial scales at which GCMs and mesoscale models operate are beginning to overlap, building physical parameterizations that could be applied both in GCMs and mesoscale models appears as crucial.

[113] A third version of the ARW-WRF model was released in April 2008, that includes the particularly interesting global mode developed in the PlanetWRF model [*Richardson et al.*, 2007], as well as adaptative time step capabilities. The evolution of the LMD Martian Mesoscale Model will benefit from these improvements, although the GCM capability is not an absolute priority, for clear reasons of redundancy with the LMD-MGCM model.

[114] At the time of writing of this paper, the two-way nesting strategy is still resulting in numerical instabilities in the LMD Martian Mesoscale Model (though the two domains are separately behaving under the CFL condition requirements). Further investigation is needed to activate this important option, which will allow us to assess the influence of mesoscale forcing on the larger-scale circulation. Besides, although no particular problems were noticed in the present study, the validity of the single-domain strategy could appear as questionable in very specific cases, even if the conditions described in section 2.3.2 are gathered. For example, the development of mesoscale circulations in conditions of large-scale baroclinic instability might be precluded by the limited extent of the mesoscale grid on the planet, because the advective time scale through the domain is then significantly smaller than the instability growth time scale. Not only the two-way nesting approach (with a large parent domain) will help solve this drawback but will also enable the analysis of the coupling between the large-scale and the mesoscale in the development of such instabilities.

4.3. Concluding Remark

[115] Martian mesoscale modeling may be seen as a physically based extrapolation of the atmospheric circulation at regional scales, from existing (sparse) measurements. As such an approach would be probably questionable on Earth, where active research is still ongoing on the topic of the initialization and validation of mesoscale models, it is less problematic on Mars for various reasons:

[116] 1. Knowledge of Martian climate is less constrained by measurements than is the case on Earth, but most of the Martian meteorological phenomena are highly repeatable in some way.

[117] 2. As stressed by *Rafkin and Michaels* [2003], the larger terrestrial atmospheric densities and radiative time scales lead to a high sensitivity of the mesoscale results to the initial state and boundary conditions, a point that is less critical on Mars.

[118] 3. Satisfactory results obtained by previous modeling studies (as well as the present one) somewhat validate the

approach that consists in relying on the mesoscale dynamical cores carefully validated on Earth, and coupling the Martian physical parameterizations designed to accurately reproduce the Martian environment as revealed by spacecraft missions and other observations.

[119] On the condition that one keeps a somewhat cautious approach about the quantitative diagnostics derived from the mesoscale models, the latter are invaluable tools to understand the Martian regional and local circulation. The numerous interesting results obtained through mesoscale modeling should not, however, conceal the need for further observational evidence to better constrain the models.

References

Antic, S., R. Laprise, B. Denis, and R. de Elía (2006), Testing the downscaling ability of a one-way nested regional climate model in regions of complex topography, *Clim. Dyn.*, *26*, 305–325.

Antonelli, M., and R. Rotunno (2007), Large-eddy simulation of the onset of the sea breeze, *J. Atmos. Sci.*, *64*, 4445–4457.

Arakawa, A. (1966), Computational design for long-term numerical integration of the equations of fluid motion: Two-dimensional incompressible flow. Part I, *J. Comput. Phys.*, *1*, 119–143.

Basu, S., M. I. Richardson, and R. J. Wilson (2004), Simulation of the Martian dust cycle with the GFDL Mars GCM, *J. Geophys. Res.*, *109*, E11006, doi:10.1029/2004JE002243.

Benson, J. L., B. P. Bonev, P. B. James, K. J. Shan, B. A. Cantor, and M. A. Caplinger (2003), The seasonal behavior of water ice clouds in the Tharsis and Valles Marineris regions of Mars: Mars Orbiter Camera observations, *Icarus*, *165*, 34–52.

Böttger, H. M., S. R. Lewis, P. L. Read, and F. Forget (2005), The effects of the Martian regolith on GCM water cycle simulations, *Icarus*, *177*, 174–189.

Carpenter, R. L., K. K. Droegemeier, P. R. Woodward, and C. E. Hane (1990), Application of the piecewise parabolic method (PPM) to meteorological modeling, *Mon. Weather Rev.*, *118*, 586–612.

Christensen, P. R., et al. (2001), Mars Global Surveyor Thermal Emission Spectrometer experiment: Investigation description and surface science results, *J. Geophys. Res.*, *106*, 23,823–23,872.

Conrath, B. J. (1975), Thermal structure of the Martian atmosphere during the dissipation of dust storm of 1971, *Icarus*, *24*, 36–46.

Dimitrijevic, M., and R. Laprise (2005), Validation of the nesting technique in a regional climate model and sensitivity tests to the resolution of the lateral boundary conditions during summer, *Clim. Dyn.*, *25*, 555–580.

Diongue, A., J. Lafore, J. Redelsperger, and R. Roca (2002), Numerical study of a Sahelian synoptic weather system: Initiation and mature stages of convection and its interactions with the large-scale dynamics, *Q. J. R. Meteorol. Soc.*, *128*, 1899–1927.

Dudhia, J. (1993), A nonhydrostatic version of the Penn State–NCAR Mesoscale Model: Validation tests and simulation of an Atlantic cyclone and cold front, *Mon. Weather Rev.*, *121*, 1493–1513.

Dufresne, J.-L., R. Fournier, C. Hourdin, and F. Hourdin (2005), Net exchange reformulation of radiative transfer in the CO_2 15-μm band on Mars, *J. Atmos. Sci.*, *62*, 3303–3319.

Fenton, L. K., A. D. Toigo, and M. I. Richardson (2005), Aeolian processes in Proctor Crater on Mars: Mesoscale modeling of dune-forming winds, *J. Geophys. Res.*, *110*, E06005, doi:10.1029/2004JE002309.

Ferri, F., P. H. Smith, M. Lemmon, and N. O. Renno (2003), Dust devils as observed by Mars Pathfinder, *J. Geophys. Res.*, *108*(E12), 5133, doi:10.1029/2000JE001421.

Forget, F. (1998), Improved optical properties of the Martian atmospheric dust for radiative transfer calculations in the infrared, *Geophys. Res. Lett.*, *25*, 1105–1109.

Forget, F., F. Hourdin, and O. Talagrand (1998), CO_2 snow fall on Mars: Simulation with a general circulation model, *Icarus*, *131*, 302–316.

Forget, F., F. Hourdin, R. Fournier, C. Hourdin, O. Talagrand, M. Collins, S. R. Lewis, P. L. Read, and J.-P. Huot (1999a), Improved general circulation models of the Martian atmosphere from the surface to above 80 km, *J. Geophys. Res.*, *104*, 24,155–24,176.

Forget, F., F. Hourdin, C. Hourdin, and O. Talagrand (1999b), Simulations of the Martian seasonal dust cycle with a general circulation model, Abstract 6206 presented at Fifth International Conference on Mars, Lunar and Planet. Inst., Pasadena, Calif.

Forget, F., R. M. Haberle, F. Montmessin, S. Cha, E. Marcq, J. Schaeffer, and Y. Wanherdrick (2003), 3D simulations of the early Mars climate with a general circulation model, Abstract 8070 presented at Third International Conference on Mars Polar Science and Exploration, Lunar and Planet. Inst., Alberta, Canada.

Forget, F., et al. (2007), Modelling the present Mars climate system as observed by Mars Express, paper presented at European Mars Science and Exploration Conference: Mars Express and ExoMars, Eur. Space Agency, Noordwijk, Netherlands.

Galperin, B. A., L. H. Kantha, S. Hassid, and A. Rosati (1988), A quasi-equilibrium turbulent energy model for geophysical flows, *J. Atmos. Sci.*, *45*, 55–62.

Gierasch, P., and C. Sagan (1971), A preliminary assessment of Martian wind regimes, *Icarus*, *14*, 312–318.

Giuranna, M., D. Grassi, V. Formisano, L. Montabone, F. Forget, and L. Zasova (2008), PFS/MEX observations of the condensing CO_2 south polar cap of Mars, *Icarus*, *197*, 386–402.

González-Galindo, F., M. A. López-Valverde, M. Angelats i Coll, and F. Forget (2005), Extension of a Martian general circulation model to thermospheric altitudes: UV heating and photochemical models, *J. Geophys. Res.*, *110*, E09008, doi:10.1029/2004JE002312.

Greeley, R., et al. (2008), Columbia Hills, Mars: Aeolian features seen from the ground and orbit, *J. Geophys. Res.*, *113*, E06S06, doi:10.1029/2007JE002971.

Haberle, R., H. C. Houben, R. Hertenstein, and T. Herdtle (1993), A boundary layer model for Mars: Comparison with Viking Lander and entry data, *J. Atmos. Sci.*, *50*, 1544–1559.

Hébrard, E., P. Coll, F. Montmessin, B. Marticorena, and G. Bergametti (2007), Modelling the aeolian erosion thresholds on Mars, in *Seventh International Conference on Mars*, *LPI Contrib. 1353*, 3144 pp., Lunar and Planet. Inst., Houston, Tex.

Hourdin, F. (1992), A new representation of the CO_2 15 μm band for a Martian general circulation model, *J. Geophys. Res.*, *97*, 18,319–18,335.

Hourdin, F., P. Le Van, F. Forget, and O. Talagrand (1993), Meteorological variability and the annual surface pressure cycle on Mars, *J. Atmos. Sci.*, *50*, 3625–3640.

Hundsdorfer, W. (1995), A positive finite-difference advection scheme, *J. Comput. Phys.*, *117*, 35–46.

Inada, A., et al. (2008), Dust haze in Valles Marineris observed by HRSC and OMEGA on board Mars Express, *J. Geophys. Res.*, *113*, E02004, doi:10.1029/2007JE002893.

Janjic, Z. I., J. P. Gerrity Jr., and S. Nickovic (2001), An alternative approach to nonhydrostatic modeling, *Mon. Weather Rev.*, *129*, 1129–1178.

Joshi, M. M., S. R. Lewis, and D. C. Catling (1995), Western boundary courrents in the Martian atmosphere: Numerical simulations and observational evidence, *J. Geophys. Res.*, *100*, 5485–5500.

Kass, D. M., J. T. Schofield, T. I. Michaels, S. C. R. Rafkin, M. I. Richardson, and A. D. Toigo (2003), Analysis of atmospheric mesoscale models for entry, descent, and landing, *J. Geophys. Res.*, *108*(E12), 8090, doi:10.1029/2003JE002065.

Klemp, J. B., W. C. Skamarock, and J. Dudhia (2007), Conservative split-explicit time integration methods for the compressible nonhydrostatic equations, *Mon. Weather Rev.*, *135*, 2897–2913.

Knievel, J. C., G. H. Bryan, and J. P. Hacker (2007), Explicit numerical diffusion in the WRF model, *Mon. Weather Rev.*, *135*, 3808–3824.

Kuzmin, R. O., R. Greeley, S. C. R. Rafkin, and R. Haberle (2001), Wind-related modification of some small impact craters on Mars, *Icarus*, *153*, 61–70.

Laprise, R. (1992), The Euler equations of motion with hydrostatic pressure as an independent variable, *Mon. Weather Rev.*, *120*, 197–207.

Lefèvre, F., S. Lebonnois, F. Montmessin, and F. Forget (2004), Three-dimensional modeling of ozone on Mars, *J. Geophys. Res.*, *109*, E07004, doi:10.1029/2004JE002268.

Lefèvre, F., J. L. Bertaux, R. T. Clancy, T. Encrenaz, K. Fast, F. Forget, S. Lebonnois, F. Montmessin, and S. Perrier (2008), Heterogeneous chemistry in the atmosphere of Mars, *Nature*, *454*, 971–975.

Leovy, C. B., G. A. Briggs, and B. A. Smith (1973), Mars atmosphere during the Mariner 9 extended mission: Television results, *J. Geophys. Res.*, *78*, 4252–4266.

Lewis, S. R., and P. L. Read (2003), Equatorial jets in the dusty Martian atmosphere, *J. Geophys. Res.*, *108*(E4), 5034, doi:10.1029/2002JE001933.

Lott, F., and M. Miller (1997), A new sub-grid scale orographic drag parametrization: Its formulation and testing, *Q. J. R. Meteorol. Soc.*, *123*, 101–128.

Madeleine, J. B., et al. (2008), Mapping water ice cloud microphysics with OMEGA/Mars Express, paper presented at Mars Water Cycle Workshop, Cent. Natl. de la Rech. Sci., Paris.

Malin, M. C., et al. (2008), Climate, weather, and north polar observations from the Mars Reconnaissance Orbiter Mars Color Imager, *Icarus*, *194*, 501–512.

Maltagliati, L., D. V. Titov, T. Encrenaz, R. Melchiorri, F. Forget, M. Garcia-Comas, H. U. Keller, Y. Langevin, and J.-P. Bibring (2008), Observations of atmospheric water vapor above the Tharsis volcanoes on Mars with the OMEGA/MEx imaging spectrometer, *Icarus*, *194*, 53–64.

Mellon, M. T., B. M. Jakosky, H. H. Kieffer, and P. R. Christensen (2000), High resolution thermal inertia mapping from the Mars Global Surveyor Thermal Emission Spectrometer, *Icarus*, *148*, 437–455.

Mellor, G. L., and T. Yamada (1982), Development of a turbulence closure model for geophysical fluid problems, *Rev. Geophys.*, *20*, 851–875.

Michaels, T. I., and S. C. R. Rafkin (2004), Large-eddy simulation of atmospheric convection on Mars, *Q. J. R. Meteorol. Soc.*, *130*, 1251–1274.

Michaels, T. I., A. Colaprete, and S. C. R. Rafkin (2006), Significant vertical water transport by mountain-induced circulations on Mars, *Geophys. Res. Lett.*, *33*, L16201, doi:10.1029/2006GL026562.

Miller, M. J., P. M. Palmer, and R. Swinbank (1989), Parametrisation and influence of sub-grid scale orography in general circulation and numerical weather prediction models, *Meteorol. Atmos. Phys.*, *40*, 84–109.

Millour, E., F. Forget, and S. R. Lewis (2008), Mars Climate Database v4.3 Detailed Design Document, Lab. de Meteorol. Dyn., Cent. Natl. d'Etudes Spatiales, Paris. (Available at http://web.lmd.jussieu.fr/forget/dvd/docs/MCD4.3_ddd.pdf)

Montabone, L., S. R. Lewis, P. L. Read, and D. P. Hinson (2006), Validation of Martian meteorological data assimilation for MGS/TES using radio occultation measurements, *Icarus*, *185*, 113–132.

Montabone, L., O. Martinez-Alvarado, A. Spiga, S. R. Lewis, P. L. Read, and F. Forget (2008), Meteorology of the 2001 Martian planet-encircling dust storm in global and mesoscale modelling with data assimilation, *Geophys. Res. Abstr.*, *10*, Abstract 10457.

Montmessin, F., F. Forget, P. Rannou, M. Cabane, and R. M. Haberle (2004), Origin and role of water ice clouds in the Martian water cycle as inferred from a general circulation model, *J. Geophys. Res.*, *109*, E10004, doi:10.1029/2004JE002284.

Montmessin, F., B. Gondet, J.-P. Bibring, Y. Langevin, P. Drossart, F. Forget, and T. Fouchet (2007), Hyperspectral imaging of convective CO_2 ice clouds in the equatorial mesosphere of Mars, *J. Geophys. Res.*, *112*, E11S90, doi:10.1029/2007JE002944.

Moudden, Y., and J. C. McConnell (2005), A new model for multiscale modeling of the Martian atmosphere, GM3, *J. Geophys. Res.*, *110*, E04001, doi:10.1029/2004JE002354.

Nayvelt, L., P. J. Gierasch, and K. H. Cook (1997), Modeling and observations of Martian stationary waves, *J. Atmos. Sci.*, *54*, 986–1013.

Newman, C. E., S. R. Lewis, P. L. Read, and F. Forget (2002), Modeling the Martian dust cycle: 1. Representations of dust transport processes, *J. Geophys. Res.*, *107*(E12), 5123, doi:10.1029/2002JE001910.

Odaka, M., K. Nakajima, S. Takehiro, M. Ishiwatari, and Y. Hayashi (1998), A numerical study of the Martian atmospheric convection with a two-dimensional anelastic model, *Earth Planets Space*, *50*, 431–437.

Palluconi, F. D., and H. H. Kieffer (1981), Thermal inertia mapping of Mars from 60°S to 60°N, *Icarus*, *45*, 415–426.

Peale, J. (1973), Water and the Martian W cloud, *Icarus*, *18*, 497–501.

Pickersgill, A. O., and G. E. Hunt (1981), An examination of the formation of linear lee waves generated by giant Martian volcanoes, *J. Atmos. Sci.*, *38*, 40–51.

Plougonven, R., A. Hertzog, and H. Teitelbaum (2008), Observations and simulations of a large-amplitude mountain wave breaking over the Antarctic Peninsula, *J. Geophys. Res.*, *113*, D16113, doi:10.1029/2007JD009739.

Putzig, N. E., and M. T. Mellon (2007), Apparent thermal inertia and the surface heterogeneity of Mars, *Icarus*, *191*, 68–94.

Rafkin, S. C. R. (2003), The effect of convective adjustment on the global circulation of Mars as simulated by a general circulation model, paper presented at Sixth International Conference on Mars, Abstract 3059, Lunar and Planet. Inst., Pasadena, Calif.

Rafkin, S. C. R., and T. I. Michaels (2003), Meteorological predictions for 2003 Mars Exploration Rover high-priority landing sites, *J. Geophys. Res.*, *108*(E12), 8091, doi:10.1029/2002JE002027.

Rafkin, S. C. R., R. M. Haberle, and T. I. Michaels (2001), The Mars Regional Atmospheric Modeling System: Model description and selected simulations, *Icarus*, *151*, 228–256.

Rafkin, S. C. R., M. R. V. Sta. Maria, and T. I. Michaels (2002), Simulation of the atmospheric thermal circulation of a Martian volcano using a mesoscale numerical model, *Nature*, *419*, 697–699.

Rafkin, S. C. R., T. I. Michaels, and R. M. Haberle (2004), Meteorological predictions for the Beagle 2 mission to Mars, *Geophys. Res. Lett.*, *31*, L01703, doi:10.1029/2003GL018966.

Rampanelli, G., D. Zardi, and R. Rotunno (2004), Mechanisms of up-valley winds, *J. Atmos. Sci.*, *61*, 3097–3111.

Raphael, M. N. (2003), The Santa Ana winds of California, *Earth Interact.*, *7*(8), 13 pp., doi:10.1175/1087-3562(2003)007<0001:TSAWOC>2.0.CO;2.

Read, P. L., and S. R. Lewis (2004), *The Martian Climate Revisited: Atmosphere and Environment of a Desert Planet*, Springer, Berlin.

Rennó, N. O., M. L. Burkett, and M. P. Larkin (1998), A simple thermodynamical theory for dust devils, *J. Atmos. Sci.*, *55*, 3244–3252.

Richardson, M. I., A. D. Toigo, and C. E. Newman (2007), PlanetWRF: A general purpose, local to global numerical model for planetary atmospheric and climate dynamics, *J. Geophys. Res.*, *112*, E09001, doi:10.1029/2006JE002825.

Savijärvi, H., and T. Siili (1993), The Martian slope and the nocturnal PBL jet, *J. Atmos. Sci.*, *50*, 77–88.

Savijärvi, H., A. Määttänen, J. Kauhanen, and A.-M. Harri (2004), Mars Pathfinder: New data and new model simulations, *Q. J. R. Meteorol. Soc.*, *130*, 669–683.

Siili, T., S. Järvenoja, J. Kauhanen, and H. Savijärvi (2006), Mars limited area model: Status report, paper presented at Second Mars Atmosphere Modelling and Observations Workshop, Lab. de Meteorol. Dyn., Granada, Spain.

Skamarock, W. C. (2006), Positive-definite and monotonic limiters for unrestricted-time-step transport schemes, *Mon. Weather Rev.*, *134*, 2241–2250.

Skamarock, W. C., and J. B. Klemp (2008), A time-split nonhydrostatic atmospheric model for weather research and forecasting applications, *J. Comput. Phys.*, *227*, 3465–3485.

Skamarock, W. C., J. B. Klemp, J. Dudhia, D. O. Gill, D. M. Barker, W. Wang, and J. G. Powers (2005), A description of the Advanced Research WRF, version 2, *NCAR Tech. Note NCAR/TN-468+STR*, Natl. Cent. for Atmos. Res., Boulder, Colo.

Smagorinsky, J. (1963), General circulation experiments with the primitive equations. I. The basic experiment, *Mon. Weather Rev.*, *91*, 99–164.

Smith, D. E., et al. (2001), Mars Orbiter Laser Altimeter: Experiment summary after the first year of global mapping of Mars, *J. Geophys. Res.*, *106*, 23,689–23,722.

Smith, M. D. (2008), Mars water vapor climatology from MGS/TES, paper presented at Mars Water Cycle Workshop, Cent. Natl. de la Rech. Sci., Paris.

Smith, M. D., M. J. Wolff, N. Spanovich, A. Ghosh, D. Banfield, P. R. Christensen, G. A. Landis, and S. W. Squyres (2006), One Martian year of atmospheric observations using MER Mini-TES, *J. Geophys. Res.*, *111*, E12S13, doi:10.1029/2006JE002770.

Sorbjan, Z. (2006), Statistics of shallow convection on Mars based on large-eddy simulations. Part 1: Shearless conditions, *Boundary Layer Meteorol.*, *123*, 121–142.

Spiga, A., and F. Forget (2008), Fast and accurate estimation of solar irradiance on Martian slopes, *Geophys. Res. Lett.*, *35*, L15201, doi:10.1029/2008GL034956.

Spiga, A., F. Forget, B. Dolla, S. Vinatier, R. Melchiorri, P. Drossart, A. Gendrin, J.-P. Bibring, Y. Langevin, and B. Gondet (2007), Remote sensing of surface pressure on Mars with the Mars Express/OMEGA spectrometer: 2. Meteorological maps, *J. Geophys. Res.*, *112*, E08S16, doi:10.1029/2006JE002870.

Stull, R. B. (1976), Internal gravity waves generated by penetrative convection, *J. Atmos. Sci.*, *33*, 1279–1286.

Tobie, G., F. Forget, and F. Lott (2003), Numerical simulation of the winter polar wave clouds observed by Mars Global Surveyor Mars Orbiter Laser Altimeter, *Icarus*, *164*, 33–49.

Toigo, A. D., and M. I. Richardson (2002), A mesoscale model for the Martian atmosphere, *J. Geophys. Res.*, *107*(E7), 5049, doi:10.1029/2000JE001489.

Toigo, A. D., and M. I. Richardson (2003), Meteorology of proposed Mars Exploration Rover landing sites, *J. Geophys. Res.*, *108*(E12), 8092, doi:10.1029/2003JE002064.

Toigo, A. D., M. I. Richardson, R. J. Wilson, H. Wang, and A. P. Ingersoll (2002), A first look at dust lifting and dust storms near the south pole of Mars with a mesoscale model, *J. Geophys. Res.*, *107*(E7), 5050, doi:10.1029/2001JE001592.

Toigo, A. D., M. I. Richardson, S. P. Ewald, and P. J. Gierasch (2003), Numerical simulation of Martian dust devils, *J. Geophys. Res.*, *108*(E6), 5047, doi:10.1029/2002JE002002.

Tyler, D., Jr., and J. R. Barnes (2005), A mesoscale model study of summertime atmospheric circulations in the north polar region of Mars, *J. Geophys. Res.*, *110*, E06007, doi:10.1029/2004JE002356.

Tyler, D., Jr., J. R. Barnes, and R. M. Haberle (2002), Simulation of surface meteorology at the Pathfinder and VL1 sites using a Mars mesoscale model, *J. Geophys. Res.*, *107*(E4), 5018, doi:10.1029/2001JE001618.

Tyler, D., Jr., J. R. Barnes, and E. Skyllingstad (2006), A new large eddy simulation model to study the convective planetary boundary layer On Mars, paper presented at Second Mars Atmosphere Modelling and Observations Workshop, Lab. de Meteorol. Dyn., Granada, Spain.

Vasavada, A. R., J.-P. Williams, D. A. Paige, K. E. Herkenhoff, N. T. Bridges, R. Greeley, B. C. Murray, D. S. Bass, and K. S. McBride (2000), Surface properties of Mars' polar layered deposits and polar landing sites, *J. Geophys. Res.*, *105*, 6961–6970.

Wang, H., and A. P. Ingersoll (2002), Martian clouds observed by Mars Global Surveyor Mars Orbiter Camera, *J. Geophys. Res.*, *107*(E10), 5078, doi:10.1029/2001JE001815.

Wicker, L. J., and W. C. Skamarock (2002), Time-splitting methods for elastic models using forward time schemes, *Mon. Weather Rev.*, *130*, 2088–2097.

Wilson, R. J. (1997), A general circulation model of the Martian polar warming, *Geophys. Res. Lett.*, *24*, 123–126.

Wilson, R. J., G. A. Neumann, and M. D. Smith (2007), Diurnal variation and radiative influence of Martian water ice clouds, *Geophys. Res. Lett.*, *34*, L02710, doi:10.1029/2006GL027976.

Wing, D. R., and G. L. Austin (2006), Description of the University of Auckland global Mars mesoscale meteorological model, *Icarus*, *185*, 370–382.

Wolff, M. J., R. T. Clancy, M. D. Smith, and MARCI Science Team, and CRISM Science Team (2008), Insights into the Mars water cycle through retrievals of aerosols and ozone: The MARCI and CRISM datasets, paper presented at Mars Water Cycle Workshop, Cent. Natl. de la Rech. Sci., Paris.

Ye, Z. J., M. Segal, and R. A. Pielke (1990), A comparative study of daytime thermally induced upslope flow on Mars and Earth, *J. Atmos. Sci.*, *47*, 612–628.

Zängl, G. (2002), An improved method for computing horizontal diffusion in a sigma-coordinate model and its application to simulations over mountainous topography, *Mon. Weather Rev.*, *130*, 1423–1432.

———————————

F. Forget and A. Spiga, Laboratoire de Météorologie Dynamique, CNRS-UPMC, BP99, 4 place Jussieu, F-75252 Paris CEDEX 05, France. (forget@lmd.jussieu.fr; spiga@lmd.jussieu.fr)